

CALIFORNIA STATE UNIVERSITY, LOS ANGELES

# **TOWARD A MEDICAL TRICORDER:**

## MACHINE LEARNING AND MICROFLUIDICS IN POINT-OF-CARE DIAGNOSTIC DEVICES

### THESIS

submitted in partial fulfillment of the requirements for graduation from the

HONORS COLLEGE

by

**Paolo Arguelles**

Approved by:

---

**DR. FRANK A. GOMEZ**, *Thesis Advisor*

---

**DR. MARLA PARKER**, *HNRS Course Instructor*

---

**DR. SCOTT WELLS**, *Honors College Associate Director*

Copyright © 2018  
Paolo Nathan M. Arguelles

**ALL RIGHTS RESERVED**

## ABSTRACT

TOWARD A MEDICAL TRICORDER:  
MACHINE LEARNING AND MICROFLUIDICS IN POINT-OF-CARE DIAGNOSTIC  
DEVICES

by Paolo Arguelles

---

### **CHAPTER 1**

The medical tricorder is introduced within the context of humanitarian use. The three subsystems of a medical tricorder-like diagnostic device are identified: *recording*, *sensing*, and *analysis*. In this chapter, three technologies that will help realize the implementation of these three subsystems in inexpensive, point-of-care applications are presented: *paper microfluidics*, *artificial intelligence*, and *digital microfluidics*. The structure of this thesis is discussed within the context of these three technologies.

---

### **CHAPTER 2**

This chapter consists of an introduction to microfluidic theory and modeling. The forces that govern passive microfluidic flow and capillary action are discussed. In this chapter, Darcy's Law governing passive fluid flow and Ohm's Law governing the passage of electrons through a conductive medium are shown to be analogous through a series of mathematical derivations. The parallelism between the functional behavior of

complex microfluidic networks and electronic circuits is therefore demonstrated. This chapter concludes that complex microfluidic networks may correctly be modeled using circuit components, and are subject to the same analysis techniques that govern electronic circuit systems.

---

## ***CHAPTER 3***

Low-cost, paper-based analytical devices that use chemical color change as an indicator of glucose concentration are especially useful in resource-limited areas. However, while users may make a qualitative self-diagnosis through color change, they lack the ability to make a more accurate, quantitative determination without the use of a spectrophotometer, an instrument used to measure color. In this research, artificial neural network-(ANN) based analytics are used to supplant the need for expensive spectrophotometric instrumentation. Color values resulting from a glucose color change reaction in two platforms, namely paper-based analytical device ( $\mu$ PAD) and paper/thread-based analytical device ( $\mu$ TPAD), were fed into classification and fitting ANNs. For the classification ANN, positive identification rates of 91.2% and 94.4% were achieved for the  $\mu$ PAD and  $\mu$ TPAD platforms, respectively. For the fitting ANN, it was found that the network yielded Pearson correlation coefficients of 0.97 and 0.96 for  $\mu$ PAD and  $\mu$ TPAD, respectively, indicating excellent ANN predictive capability for both platforms.

## **CHAPTER 4**

---

Scholarly discussion of the realization of logic gates in microfluidic networks often involve their active implementation through the use of bubble logic or peristaltic micro-pumps. In this chapter, a method for implementing logical operations on microfluidic networks *passively* is described. The behavior of a passive half-adder is realized using basic acid-base stoichiometry and phenolphthalein indicator. Color is toggled by continuously and strategically breaching the pH threshold at which phenolphthalein turns pink. The absence or presence of color (logic-0 and logic-1, respectively) is interpreted as a binary system. Preliminary results conducted in an ideal mixing scenario are detailed, and a vision of a passive microfluidic-based calculator presented.

## **CHAPTER 5**

---

The field of digital microfluidics is introduced, and a novel digital microfluidic paper-based analytical device (D $\mu$ PAD) proposed. In the present research, photolithographic etching methods were used to create electrode arrays. Commercially available hydrophobic spray was applied onto a Parafilm dielectric to facilitate smooth droplet actuation over the electrode array. In this research, circuit etching and hydrophobic coating methodologies were perfected, and procedures described. The droplet actuation voltage associated with the electrode array preparation methods described herein was found to be +200 VDC. An array of logic-level BSP89 power

metal-oxide-semiconductor field-effect transistors (MOSFETs) were used to control a +200 VDC bus line to each electrode. Switching states are controlled over the +5 VDC logic bus on an Arduino Uno. Future applications of electrowetting-on-dielectric (EWOD) based technology are described, including possible integration with a paper-based enzyme-linked immunosorbent assay (ELISA).

## ACKNOWLEDGMENTS

This thesis represents the culmination of two years of highly interdisciplinary research work with the Microfluidics and Point-of-Care Diagnostics Research Laboratory supervised by Dr. Frank A. Gomez. I would like to acknowledge and thank Dr. Gomez for his mentorship throughout my tenure in his research lab. My time there has resulted in my working on several interdisciplinary efforts at the intersection of electrical engineering and chemistry, as well culminated in the publication of my first academic paper and the writing of this thesis. My experience in Dr. Gomez's lab has been integral to my success in my graduate school applications and my admittance into ten world-renowned EECS graduate programs, from which I have chosen to pursue an M.Eng. in Electrical and Computer Engineering at Cornell University. I will never forget the kindness and generosity shown to me not only by Dr. Gomez, but also by all the friends I have made in his research group.

I would also like to thank Dr. Deborah S. Won, my primary mentor in the fields of electrical and biomedical engineering; Dr. Lili Tabrizi; as well as the rest of the Department of Electrical and Computer Engineering. I would also like to acknowledge Ted Nye and Dr. Michael Thorburn for spearheading a wonderful Senior Design Program.

I would also like to thank Dr. Richard S. Maddox, Isabelle Garcia, and the rest of the Early Entrance Program community. I would especially like to acknowledge Dr.

Maddox for his more than 20 years of service and dedication to the Early Entrance Program, and the gifted youth community. I am grateful to have been part of the Program under his directorship for the past five years. I sincerely hope that the future of the Early Entrance Program at Cal State LA will be a bright one.

I also wish to acknowledge the Honors College, especially Dr. Trinh Pham, Jessica Rodriguez, Cassidy Zimmerman, Dr. Martin Adamian, Dr. Jose Anguiano, Dr. Scott Wells, Dr. Michelle Hawley and Dr. Marla Parker. The Honors College family has been integral to my success at Cal State LA. My experience as an Honors student has afforded me an Edison Scholarship, Honors College Scholarship, a 2016 Honorable Mention from the Barry Goldwater Scholarship Foundation, the opportunity to travel to several academic conferences, as well as the completion of this thesis. I will greatly miss the Honors College community, and all the support it provided me during my time at Cal State LA.

I would also like to thank the Pat Brown Institute for Public Affairs for instilling within me a commitment to civic engagement, public policy, and the public good over the past academic year. I am grateful to Dr. Raphael Sonenshein, Raquel Beltrán, Dr. Max Baumgarten, and Lily Baba for enabling me to exercise my skillset in electrical engineering in a more social- and civic-minded context. I wish the Pat Brown Institute all the best in its continuing commitment to “unleashing the power of participation,” both in our campus community, and in our city.

Lastly, I wish to dedicate this thesis to my mom, dad, and Lola, who have always supported me in all that I do.

# CONTENTS

<b>ABSTRACT</b>	<i>iv</i>
<b>ACKNOWLEDGMENTS</b>	<i>vii</i>
<b>LIST OF FIGURES</b>	<i>xi</i>
<b>CHAPTER 1. INTRODUCTION</b>	<b>1</b>
<i>1.1. The Medical Tricorder</i>	<i>1</i>
1.1.1. Device Structure	<i>1</i>
1.1.2. Humanitarian Uses	<i>2</i>
<i>1.2. Thesis Overview</i>	<i>3</i>
<i>REFERENCES</i>	<i>5</i>
<b>CHAPTER 2. MICROFLUIDIC THEORY AND MODELING</b>	<b>7</b>
<i>2.1. Microfluidic Theory</i>	<i>5</i>
2.1.1. Circuit Equivalent Models of Microfluidic Networks	<i>10</i>
2.1.2. Applying Circuit Analysis to Microfluidic Networks	<i>13</i>
<i>REFERENCES</i>	<i>15</i>
<b>CHAPTER 3. MACHINE LEARNING IN PAPER MICROFLUIDICS</b>	<b>17</b>
<i>3.1. Introduction</i>	<i>17</i>
3.1.1. Artificial Neural Networks (ANN)	<i>17</i>
3.1.2. Microfluidic Paper- and Paper/Thread-Based Analytical Devices	<i>19</i>
3.1.3. Using ANN to Aid Color-Based Diagnostics	<i>20</i>
3.1.4. Existing Work	<i>24</i>
<i>3.2. Experimental Methods</i>	<i>25</i>
3.2.1. Normalizing Color and Lighting Conditions	<i>25</i>
3.2.2. Artificial Neural Network Training Methodology	<i>26</i>
<i>3.3. Results and Discussion</i>	<i>14</i>
3.3.1. ANN Predictive Performance for $\mu$ TPAD Platform	<i>35</i>
3.3.2. ANN Predictive Performance for $\mu$ PAD Platform	<i>37</i>
<i>3.4. Concluding Remarks</i>	<i>38</i>
<i>REFERENCES</i>	<i>40</i>

---

**CHAPTER 4. PASSIVE LOGIC ON PAPER MICROFLUIDICS** **42**

4.1.	<i>Introduction</i>	42
4.2.	<i>Experimental Methods</i>	45
4.2.1.	Phenolphthalein as an Indicator of Basicity	45
4.2.2.	Implementing the Half-Adder	46
4.3.	<i>Results and Discussion (Preliminary)</i>	47
4.4.	<i>Concluding Remarks</i>	48
	<i>REFERENCES</i>	49

---

**CHAPTER 5. DIGITAL MICROFLUIDIC PAPER ANALYTICAL DEVICES** **50**

5.1.	<i>Introduction</i>	50
5.1.1.	The Electrowetting-on-Dielectric Phenomenon in DMF Devices	50
5.1.2.	Electrowetting Theory	52
5.1.3.	Contact Angle Saturation	54
5.1.4.	Droplet Operation Types	55
5.1.5.	DMF Device Configurations	55
5.1.6.	The D $\mu$ PAD	56
5.2.	<i>Experimental Methods</i>	56
5.2.1.	Creating the Electrode Array	56
5.2.2.	Creating the Hydrophobic Dielectric Layer	60
5.2.3.	Designing the Electrode Array Circuitry	61
5.3.	<i>Results and Discussion (Preliminary)</i>	62
5.4.	<i>Concluding Remarks</i>	63
5.4.1.	DMF-Enabled ELISA Microsystem	63
	<i>REFERENCES</i>	66

# LIST OF FIGURES

---

## ***CHAPTER 1***

---

1.1.	The medical tricorder as seen in the original Star Trek television series	1
1.2.	Rural regions of central Africa disappear in this geographic projection of global 2018 GDP.	2

---

## ***CHAPTER 2***

---

2.1.	Fluidic flux $Q$ is a function of cross-sectional area $A$ and length $L$ . <i>(Attrib.: Peter Kapitola)</i>	10
2.2.	A microfluidic network (left) and its corresponding circuit model equivalent (right)	14

---

## ***CHAPTER 3***

---

3.1.	Schematic of a simple three-input perceptron	17
3.2.	Plot of the Heaviside step function	18
3.3.	Plot of the sigmoid activation function	18
3.4.	The nonlinear, sigmoidal relationship between yellow channel intensity and glucose concentration	20
3.5.	Most color change occurs along the yellow color channel in this reaction.	21
3.6.	Scatter plot depicting cross entropy among concentration categories	23
3.7.	A manually labeled image of a microfluidic test strip/array	25
3.8.	Neural network topology for regression	27
3.9.	Internal block diagram for an active, hidden layer node	28
3.10.	Internal block diagram for an active, output layer node in a linear regression problem	29
3.11.	Custom Simulink GUI for fitting problem	30
3.12.	Neural network topology for classification	32
3.13.	Custom Simulink GUI for classification problem	33

3.14.	(A) Regression plot for $\mu$ TPAD neural network fitting program, (B) Regression plot for $\mu$ PAD neural network fitting program, (C) Confusion matrix for $\mu$ TPAD neural network classification program, (D) Confusion matrix for $\mu$ PAD neural network classification program	34
3.15.	Internal block diagram of an active, output layer node in a classification problem	35

---

#### ***CHAPTER 4***

4.1.	A four-bit domino adder	42
4.2.	Circuit diagram for a conventional half-adder	43
4.3.	Behavior for a half-adder	43
4.4.	(A) The dynamics of the “S” test area (not to scale), (B) the dynamics of the “C” test area (not to scale)	45
4.5	A 1.0 $\mu$ L solution of 13.5 NaOH acts as the pre-spotted output “S” area ( <i>top left</i> ), one aliquot of 0.5 $\mu$ L of equal parts phenolphthalein and vinegar is added to the solution ( <i>top middle</i> ), producing color ( <i>top right</i> ). Another aliquot of input solution is added to the colored mixture ( <i>bottom left</i> ), producing a colorless mixture ( <i>bottom middle, right</i> ).	47

---

#### ***CHAPTER 5***

5.1.	Water droplets with contact angles of (left) 120°, (middle) 90°, and (right) 50°	51
5.2.	The triphasic boundary in the electrowetting model showing relevant quantities	53
5.3.	Saturation <i>velocity vs. contact angle</i> curves, controlled by applied actuation voltage	54
5.4.	An EWOD device in <i>sandwich</i> (left) and <i>open-faced</i> (right) configurations	55
5.5.	The transparent mask used for PCB photoresist etching	57
5.6.	Configuration of the presensitized PCB, transparent mask, and glass slide during the exposure step of the photolithography process	58
5.7.	The exposed PCB is developed via sodium hydroxide (NaOH) immersion	58

5.8.	The photosensitized PCB is immersed in ferric chloride etching solution.	<b>59</b>
5.9.	Acetone is swabbed on the etched board to remove the remaining photoresist film and complete the photolithography process.	<b>59</b>
5.10.	Custom PCB for DMF electrode array. ( <i>Design by Nico Pierson</i> )	<b>62</b>
5.11.	Circuit schematic of a DMF electrode array. ( <i>Design by Nico Pierson</i> )	<b>63</b>

# CHAPTER 1.

## INTRODUCTION

### 1.1. THE MEDICAL TRICORDER

#### 1.1.1. Device Structure

Originally the product of popular science fiction, the real world implementation of the *medical tricorder* constitutes one of the most coveted prizes for biomedical and electrical engineers [2, 6]. The fabled device is depicted to non invasively scan biological specimens and diagnose conditions such as arrhythmia, diabetes, and sleep apnea [9]. The medical *tricorder*, short for *tri-functional recorder*, is named for the three functional subsystems that comprise the device: *sensing*, *analysis*, and *recording*.

The *sensing* subsystem is concerned with

the development of novel sensing methods, and miniaturized, biocompatible sensors and sensing arrays; *analysis* with the signal processing methods and algorithms to facilitate accurate diagnostic capability; and *recording* with data storage methods and circuitry to enable high sampling rate, multivariate, multi-channel recording. This thesis focuses primarily on the development of techniques supplement *sensing* and *analysis*.



**Figure 1.1.** The medical tricorder as seen in the original *Star Trek* television series

### 1.1.2. Humanitarian Uses

This research work is motivated by a humanitarian element, specifically the potential use of this device in resource-limited areas, regions of the world loosely defined here as those that do not have the benefit of a robust health care infrastructure. The need for a point-of-care diagnostic device designed for use in these areas is especially evident considering that approximately 60% of the world's population lives in resource-limited areas [4]. Figure 1.1 depicts the distribution of global wealth, with countries resized

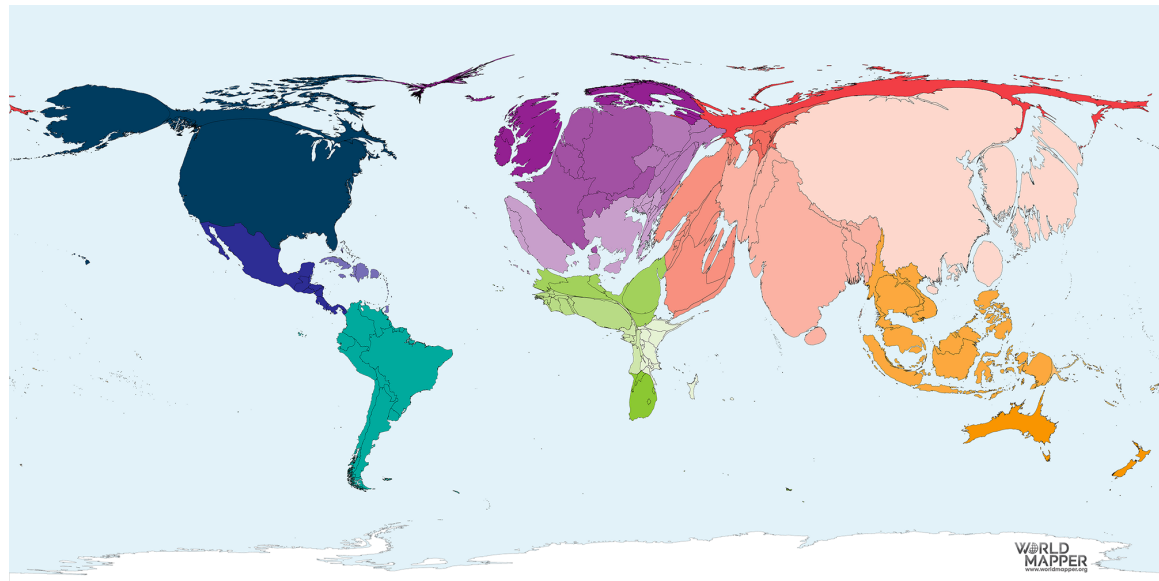


**Figure 1.2.** Rural regions of central Africa disappear in this geographic projection of global 2018 GDP.

according to their 2018 GDP. Wealth has been shown to act as an indicator of that country's ability to support a vast, robust medical infrastructure [3, 5]. A 2010 report by the World Health Organization paints a dire picture of the financing of health care infrastructure in rural Africa:

The financing of healthcare in Africa remains a patchwork of meagre public spending, heavy reliance on foreign donors and a large dependence on out-of-pocket contributions and user fees that place the greatest burden on the poorest members of society [1].

Given a clear need for inexpensive, yet robust medical diagnostic capability in resource-limited areas, this thesis will discuss technologies that will support the creation of a medical tricorder-like point-of-care diagnostic device designed specifically for such regions. Toward this end, such a device should not only be able to provide quality, accurate diagnoses, but do so while minimizing expense. Recent advances in paper-based microfluidics and machine learning provide support for the inexpensive implementation of the *sensing* and *analysis* subsystems, respectively, of point-of-care diagnostic instrumentation [15-24]. Chemical sensors and assays may be fashioned out of chemically enriched paper and wax for only a few cents [8-14], making such platforms ideal for use in resource-limited areas [7]. Similarly, machine learning algorithms may be accessed by regional caregivers over the internet. The integration of these two disciplines constitutes the main area of this thesis.

## 1.2. THESIS OVERVIEW

This thesis is built upon advances in three emergent technologies that: paper microfluidics (PMF), digital microfluidics (DMF), and artificial intelligence (AI). The

letter combinations in parentheses indicate which technologies are addressed in each chapter.

**CHAPTER 1** consisted of an introduction to the medical tricorder, and the importance of inexpensive, point-of-care diagnostic systems in resource-limited areas.

**CHAPTER 2** discusses microfluidic theory and the modeling of active and passive microfluidic networks as electrical circuits.

*(Technologies: PMF)*

**CHAPTER 3** will consist of an application of machine learning techniques to a problem in microfluidics and point-of-care diagnostics. In particular, artificial neural networks (ANN) are used to evaluate colorimetric data from a completed assay and predict the corresponding glucose concentration.

*(Technologies: PMF, AI)*

**CHAPTER 4** discusses the implementation of simple logical operations onto passive microfluidics. Additionally, the theoretical operation of a half adder circuit is related to microfluidic network topology.

*(Technologies: PMF)*

**CHAPTER 5** proposes a microfluidic paper analytical device with digital microfluidic capability. The electrowetting-on-dielectric (EWOD) is described, and applied to microfluidic devices. An enzyme-linked immunosorbent assay (ELISA) employing this capability is discussed.

*(Technologies: PMF, DMF)*

## REFERENCES

1. Fenny, A. P.; Asante, F. A.; Enemark, U.; Hansen, K. S. *Global Journal of Health Science* 2014, 7 (1).
2. Gavriel, C.; Parker, K. H.; Faisal, A. A. *2015 IEEE 12th International Conference on Wearable and Implantable Body Sensor Networks (BSN)* 2015.
3. Mills, A.; Ataguba, J. E.; Akazili, J.; Borghi, J.; Garshong, B.; Makawia, S.; Mtei, G.; Harris, B.; Macha, J.; Meheus, F.; McIntyre, D. *The Lancet* 2012, 380 (9837), 126–133.
4. Overview <http://www.worldbank.org/en/topic/poverty/overview> (accessed Apr 18, 2018).
5. Tanser, F.; Gijsbertsen, B.; Herbst, K. *Social Science & Medicine* 2006, 63 (3), 691–705.
6. Waters, H. *Nature Medicine* 2011, 17 (7), 754–754.
7. Syedmoradi, L., Gomez, F. A., *Bioanalysis*, 2017, 9, 841-843.
8. Martinez, A. W., Phillips, S.T., Butte, M. J., Whitesides, G. M., *Angew. Chem., Int. Ed.* 2007, 46, 1318–1320.
9. Martinez, A.W., Phillips S. T., Carrilho, E., Thomas III, S. W., Sindi, H., Whitesides, G. M., *Anal. Chem.* 2008, 80, 3699–3707.
10. Bruzewicz, D. A., Reches, M., Whitesides, G. M., *Anal. Chem.* 2008, 80, 3387-3392.
11. Martinez, A. W., Phillips, S. T., Wiley, B. J., Gupta, M., Whitesides, G. M., *Lab Chip* 2008, 8, 2146–2150.
12. Martinez, A. W., Phillips, S. T., Whitesides, G. M., Carrilho, E., *Anal. Chem.* 2010, 82, 3-10.
13. Schilling, K. M., Lepore, A. L., Kurian, J. A., Martinez, A.W., *Anal. Chem.* 2012, 84, 1579–1585.

14. Cheng, C. M., Mazzeo, A. D., Gong, J. L., Martinez, A. W., Phillips, S .T., Jain, N., Whitesides, G. M., *Lab Chip* 2010, *10*, 3201–3205.
15. Rodriguez, N. M., Wong, W. S., Liu, L., Dewar, R., Klapperich, C. M., *Lab Chip*, 2016, *16*, 753–763.
16. Kim, W. S., Shin, J. H., Park, H. K., Choi, S., *Sensor Actuat. B Chem.* 2016, *222*, 1112–1118.
17. Ueland, M., Blanes, L., Taudte, R.V., Stuart, B. H., Cole, N., Willis, P., Roux, C., Doble, P., *J. Chromatogr. A*, 2016, 1436, 28–33.
18. Jang, I., Song, S., *Lab Chip* 2015, *15*, 3405-3412.
19. Zhang, Y., Zuo, P., Ye, B. C., *Biosens. Bioelectron.* 2015, *68*, 14-19.
20. Jin, S. Q., Guo, S. M., Zuo, P., Ye, B. C., *Biosens. Bioelectron.* 2015, *63*, 379–383.
21. Yang X., Reavis, H. D., Roberts, C. L., Kim, J. S., *Anal. Chem.* 2016, *88*, 7904-7909.
22. Park, T. S., Li, W., McCracken, K. E., Yoon, J. -Y., *Lab Chip* 2013, *13*, 4832-4840.
23. Ferrer, I. M., Valadez, H., Estala L., Gomez F.A., *Electrophoresis* 2014, *35*, 2417-2419.
24. Renault, C., Koehne, J., Ricco, A. J., Crooks, R. M., *Langmuir* 2014, *30*, 7030-7036.

## CHAPTER 2.

### MICROFLUIDIC THEORY AND MODELING

#### 2.1. MICROFLUIDIC THEORY

Microfluidics is a field of study having to do with the manipulation of fluid volumes on the order of nanoliter ( $10^{-9}$ ) to picoliter ( $10^{-12}$ ) aliquots on or within a substrate [8]. Passive microfluidic systems, such as those implemented on paper or thread, are characterized by capillary action, or the ability of a fluid to flow within a porous medium against the wishes of external forces such as gravity, as the primary driver of fluidic flow [9]. Passive microfluidics will be the primary focus of the thesis. For a conventional porous medium, the volume of fluid wicked from a reservoir through capillary action over time is expressed as a decaying exponential:

$$V_{\text{absorbed}} \propto A\sqrt{t} \quad (2.1)$$

where  $V_{\text{absorbed}}$  is the volume of liquid absorbed after a time  $t$ , and  $A$  is the cross-sectional area of the wicking material. A proportionality constant  $S$  is defined as the *sorptivity* of the material [11].

The most fundamental relationship governing passive fluidic flow in porous media was found in the context of hydrogeology [2]. Henry Darcy studied the dynamics of groundwater flow through sediment, formulating his namesake relation

$$q \propto -\nabla p. \quad (2.2)$$

Darcy's Law states that fluid flow flux  $q$  in m/s is inversely proportional to the pressure gradient  $\nabla p$  in Pa/m<sup>2</sup>, leading to two trivial conclusions:

1. Fluidic flow occurs in the direction of high to low pressure.
2. The larger the pressure difference, the greater the fluid flow.

Darcian fluid flow flux can be used to compute the Reynold's number for passive flow, given by

$$\mathcal{R}_{passive} = \frac{\rho q d}{\mu} \quad (2.3)$$

where  $\rho$  is fluid density ( $\rho = 1$  g/mL for water),  $q$  is the Darcian fluid flow flux derived in Equation 2.2, and  $d$  is the average "grain size" for the porous medium. For microfluidic systems implemented passively on paper and thread, or actively on PDMS,

$$\mathcal{R}_{passive} \lesssim 1.0 \quad (2.4)$$

where  $\mathcal{R} = 0$  represents perfectly laminar flow. It is generally assumed that the Reynolds number in microfluidic chips is negligible, and that fluidic flow is laminar. Two of the quantities describing fluid flow dynamics, namely *flux* and *velocity* are related by *porosity*  $\Phi$  as follows

$$\Phi = \frac{q}{v} \quad (2.5)$$

When implementing a circuit model equivalent for microfluidic systems, a channel is best modeled as a resistor, with resistance analogous to porosity. Parallels may immediately be drawn with Ohm's Law in its original formulation:

$$\sigma = \frac{J}{E} \quad (2.6)$$

where  $J$  is current density in A/m<sup>2</sup>, and  $E$  is electric field strength in V/m. The most famous version of Ohm's Law as modified by Gustav Kirchhoff, given by

$$R = \frac{V}{I} \quad (2.7)$$

shows an inverse linear correlation between the resistance of a wire and the current flowing through it. For a length of ideal wire, resistance  $R$  is given by

$$R = \frac{\rho L}{A} \quad (2.8)$$

where  $\rho$  is the resistivity of the material from which the wire is made (for copper,  $\rho_{Cu} = 1.7 \times 10^{-6} \Omega\text{m}$ ),  $L$  is the length of the wire and  $A$  is cross-sectional area. More generally, the following relationship between resistance and wire dimensions can be extracted:

$$R \propto \frac{L}{A} \quad (2.9)$$

When *resistance* is replaced with *porosity*, the same relationship holds for a porous medium with a low Reynolds number [2]:

$$\Phi \propto \frac{L}{A} \quad (2.10)$$

For paper microfluidic systems, the physical interpretation of porosity is dictated by the amount of wax melted into the paper. When designing paper microfluidics on vector

illustration software, this porosity is controlled by the *opacity* of the region. A region with 100% opacity (wax barrier, completely opaque) is analogous to an infinite, or very high, resistance, while a region with 0% opacity (no wax printed, completely clear) corresponds to an ideal wire with zero resistance. A helpful analogy is that the opacity percentage value indicates the extent to which floodgates are open to allow a deluge to flow within a canal. Here, the water corresponds to fluidic flow, the floodgates to the porosity of the regions, and the canal to the porous micro-channel.

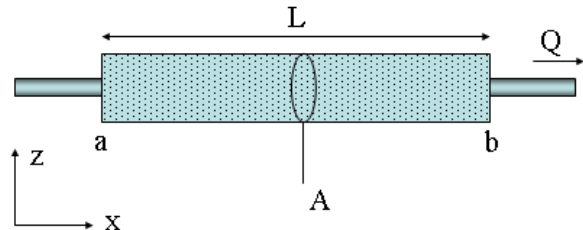


**Figure 2.1.** Fluidic flux  $Q$  is a function of cross-sectional area  $A$  and length  $L$ . The dependence of flux on dimensions substrate is mirrored in the electron current flow of an ideal wire, shown in Equations (2.9) and (2.10). (*Attrib.: Peter Kapitola*)

### 2.1.1. Circuit Equivalent Models of Microfluidic Networks

While it was shown that resistance can be used to model paper microfluidic micro-channels, other circuit components can be used to model more complex microfluidic chip topologies. Circuit equivalent models of the cardiovascular system, for instance, incorporate *inductance*, a circuit component used to simulate the inertia of blood as it travels through the vasculature, as follows:

$$L_{vessel} = \frac{9l\rho}{4A} \quad (2.11)$$

where  $\rho$  is the density of blood [1]. It should be noted that for microfluidic systems using fluids with low viscosities, or that are under the influence of a constant propulsive vector, inductance plays a negligible role in determining that system's circuit equivalent. In general, for microfluidics implemented actively on PDMS, or passively on paper and thread substrates, fluid inertia is not an important contributor to the behavior of the system. On the other hand, capacitance is used to model the compliance or elasticity of the blood vessel wall:

$$C_{vessel} = \frac{3l\pi r^3}{2Ew} \quad (2.12)$$

where  $r$  and  $l$  are blood vessel radius and length respectively,  $E$  is Young's modulus, and  $w$  is the blood vessel wall thickness [1].

Consider an ideal section of compliant tubing. While the relationship between the difference in fluid flux  $F$  and the difference in pressures  $P$  at the input and output is nonlinear, for a channel exhibiting laminar flow, these two quantities may be taken to be directly proportional:

$$F \propto P. \quad (2.13)$$

Differentiating both sides,

$$\frac{dF}{dt} \propto \frac{dP}{dt} \quad (2.14)$$

and defining a new variable  $A$ , denoting the change in flux,

$$A = \frac{dF}{dt} \quad (2.15)$$

it may be written:

$$A = k \frac{dP}{dt} \quad (2.16)$$

where  $k$  is some proportionality constant. Now, recall the behavior of a current  $I$  through a capacitor:

$$I = C \frac{dV}{dt} \quad (2.17)$$

where  $C$  is the capacitance, and  $V$  is the voltage across the capacitor. Notice the similarity in form between the two previous equations. This equivalence shows that a capacitor may be used to model a channel that changes its dimensions based on fluidic flow.

Given the equivalencies between microfluidic systems and electronic circuitry, it is conceivable that active microfluidic systems can perform any logical operation an electronic circuit can [4, 5, 7, 10]. The microfluidic implementation of logic gates is discussed in Chapter 3. However, PDMS micro-channels and wax channels printed onto paper are usually not subject to such compliance. These networks can be sufficiently modeled using a network of voltage sources and resistors [6, 8]. For PDMS-based microfluidics that use peristaltic pumps or some other method of external actuation of fluid flow, a time-dependent voltage source is suitable [3]. For simple, passive, paper-and thread-based microfluidic platforms such as those discussed in this thesis, a constant DC voltage source may be used to describe pressure gradients that govern fluidic flow via capillary action in the system [6].

### 2.1.2. Applying Circuit Analysis to Microfluidic Networks

According to Ampere's and Gauss's Laws, charge within an isolated system is always conserved. A consequence of this conservation of charge, Kirchhoff's Current Law (KCL), is given by

$$\sum I_n = 0 \quad (2.18)$$

where  $I$  is the current through branch  $n$  and the total number of branches entering a junction is  $N$ . KCL states trivially that the summation of all currents entering a junction must equal zero. For active microfluidic systems implemented on PDMS, such circuit laws can be used to model fluid behavior given channel topology [6, 7]. Conversely, circuit analysis methods may be used to optimize microfluidic channel topology to achieve a desired fluid behavior. KCL may be rewritten in terms of microfluidic networks using fluid flux  $Q$ :

$$\sum Q_n = 0 \quad (2.19)$$

Another consequence of the conservation of charge is Kirchhoff's Voltage Law (KVL), given by:

$$\sum V_n = 0 \quad (2.20)$$

KVL states that the algebraic sum of all voltage drops in a closed path equal zero. Since voltage is analogous to pressure in microfluidic networks, KVL may be rewritten in this context as:

$$\sum P_n = 0 \quad (2.21)$$

The theoretical equivalence Kirchhoff's Laws to microfluidic networks render the latter able to be analyzed with the same tools and methods used to conduct circuit analysis, save for a few conceptual adjustments. As such, software normally reserved for electrical engineering and circuit analysis (i.e., *PSpice*, *LTS spice*, *Simscape Electronics*) may be used to model time-dependent microfluidic behavior on a macroscopic scale.

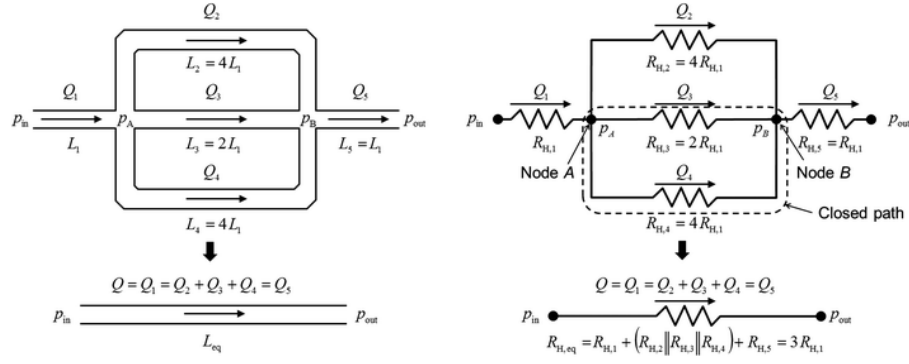


**Figure 2.2.** A microfluidic network (left) and its corresponding circuit model equivalent (right) [6]

## REFERENCES

1. Abdolrazaghi, M.; Navidbakhsh, M.; Hassani, K. *Cardiovascular Engineering* 2010, 10 (2), 45.
2. Bruus, H. *Microscale Acoustofluidics* 1.
3. Cummins, B. M.; Chinthapatla, R.; Ligler, F. S.; Walker, G. M. *Analytical Chemistry* 2017, 89 (8), 4377.
4. Grover, W. H.; Ivester, R. H. C.; Jensen, E. C.; Mathies, R. A. *Lab on a Chip* 2006, 6 (5), 623.
5. Hassani, K.; Navidbakhsh, M.; Rostami, M. *Biomedical Papers* 2006, 150 (1), 105.
6. Oh, K. W.; Lee, K.; Ahn, B.; Furlani, E. P. *Lab on a Chip* 2012, 12 (3), 515.
7. Prakash, M.; Gershenfeld, N. *Science* 2007, 315 (5813), 832.
8. Squires, T. M.; Quake, S. R. *Reviews of Modern Physics* 2005, 77 (3), 977.
9. Vestad, T.; Marr, D. W. M.; Munakata, T. *Applied Physics Letters* 2004, 84 (25), 5074.
10. Whitaker, S. *Transport in Porous Media* 1986, 1 (1), 3.
11. Zhong, W. *Thermal and Moisture Transport in Fibrous Materials* 2006, 136.
12. Martinez, A. W., Phillips, S.T., Butte, M. J., Whitesides, G. M., Angew. *Chem., Int. Ed.* 2007, 46, 1318–1320.
13. Martinez, A.W., Phillips S. T., Carrilho, E., Thomas III, S. W., Sindi, H., Whitesides, G. M., *Anal. Chem.* 2008, 80, 3699–3707.
14. Bruzewicz, D. A., Reches, M., Whitesides, G. M., *Anal. Chem.* 2008, 80, 3387-3392.
15. Martinez, A. W., Phillips, S. T., Wiley, B. J., Gupta, M., Whitesides, G. M., *Lab Chip* 2008, 8, 2146–2150.

16. Martinez, A. W., Phillips, S. T., Whitesides, G. M., Carrilho, E., *Anal. Chem.* 2010, 82, 3-10.
17. Schilling, K. M., Lepore, A. L., Kurian, J. A., Martinez, A. W., *Anal. Chem.* 2012, 84, 1579–1585.
18. Cheng, C. M., Mazzeo, A. D., Gong, J. L., Martinez, A. W., Phillips, S. T., Jain, N., Whitesides, G. M., *Lab Chip* 2010, 10, 3201–3205.

# CHAPTER 3.

## MACHINE LEARNING IN PAPER MICROFLUIDICS

### 3.1. INTRODUCTION

#### 3.1.1. Artificial Neural Networks (ANN)

Inspired by the biological workings of the brain, an artificial neural network (ANN) is an interconnected group of electronic nodes that performs decision-making functions [5]. ANNs may be seen as a kind of artificial intelligence [1-3]. The simplest artificial neuron is called a *perceptron*, an algorithm that outputs either 1 or 0 based on a series of input variables. For instance, consider a typical yes or no decision: going to the gym. This decision depends on the consensus of multiple variables. A few contributing factors might be weather  $x_1$ , mood  $x_2$ , and time of day  $x_3$ . These variables may be fed into a perceptron as follows:

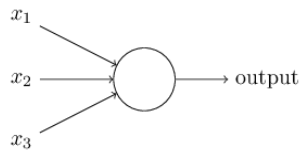


**Figure 3.1.** Schematic of a simple three-input perceptron

One may consider their mood to contribute more to their decision than weather or time of day; greater weight is applied to this variable over the others. The weighted sum is then introduced to the Heaviside step function which acts as follows: if the weighted sum exceeds a certain threshold, the perceptron will output a 1 (analogous to the firing of a

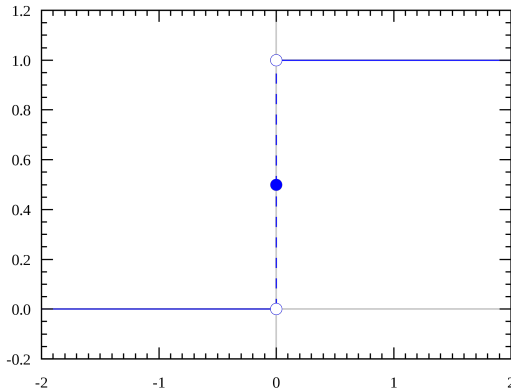


**Figure 3.2.** Plot of the Heaviside step function

neuron); otherwise, the perceptron will remain inactive, outputting a 0 [6]. By altering the shape of the activation function from a sharp, discontinuous step to a smoothed out curve, more subtle decisions (as opposed to a discrete yes or no decision) can be made. One such curve shown in Figure 3.3 is a sigmoid function, characterized by  $f(x) = \frac{1}{1 + e^{-x}}$ .

In conventional ANNs, the sigmoid function, or a similar-shaped curve, is used as the

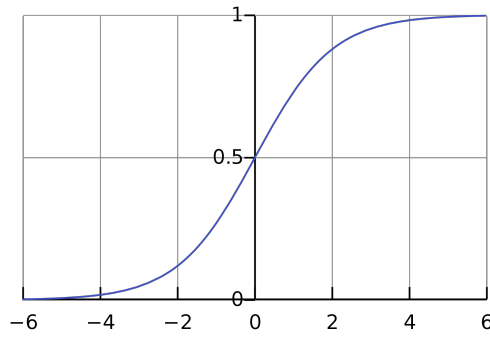


**Figure 3.3.** Plot of the sigmoid activation function

activation function. By creating an interconnected network multiple sigmoid neurons, and

adding multiple layers of neurons to mimic abstract thought, very complex decisions may be made based upon hundreds of input factors.

To train the ANN, a database of input and output data is introduced to the system. In a training algorithm called “backpropagation,” the error (the difference between the actual output and the expected output) is calculated and “backpropagates” to earlier neurons, whose weights are then adjusted accordingly. This procedure is performed multiple times to minimize error.

### *3.1.2. Microfluidic Paper- and Paper/Thread-Based Analytical Devices*

Low-cost medical diagnostic devices may be fashioned out of paper, wax, thread, and tape. For microfluidic paper-based analytical devices ( $\mu$ PADs) hydrophobic channels can be created using wax printers and paper. When a desired design is printed onto paper, a heat press dissolves the wax into the paper, creating hydrophobic barriers that constrain fluid flow within the paper. Other topologies may be explored, such as microfluidic paper/thread-based analytical devices ( $\mu$ TPADs); channels are created by pieces of thread that allow fluids to propagate to different test areas.

In this chapter, ANNs will be applied to the colorimetric determination [14, 15] of glucose concentration in an artificial urine solution. The objective of the machine learning program is to learn the highly nonlinear relationship [4] between color and glucose concentration, and output a glucose concentration value given a set of color inputs. The input solution consists of a cocktail of horseradish peroxidase (HRP),

potassium iodide (KI), and glucose oxidase (GOx). The capillarity of the paper allows the input solution to flow onto each of the test areas containing predetermined concentrations of glucose in an artificial urine solution, facilitating a color change reaction. Depending on glucose concentration, the test area will assume different shades of yellow at varying saturation levels—clear to pale yellow for low glucose concentrations, and dark brown for high concentrations.

### 3.1.3. Using ANN to Aid Color-Based Diagnostics

The challenges of achieving highly accurate colorimetric analytical capability in paper-based assays without the aid of expensive color-detecting instruments such as

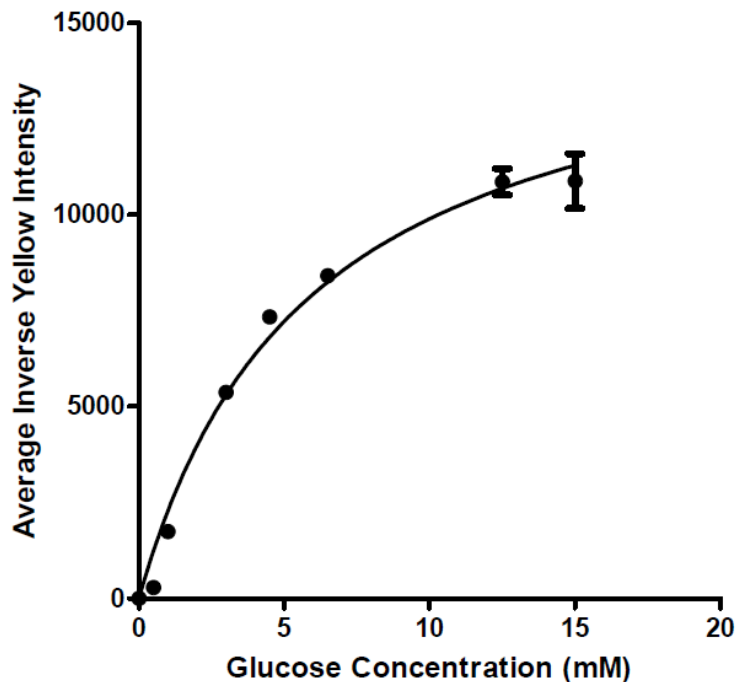


**Figure 3.4.** The nonlinear, sigmoidal relationship between yellow channel intensity and glucose concentration

spectrophotometers highlight the benefits of a machine learning-based approach to such problems. Firstly, the highly nonlinear nature of the relationship between color data and concentration is one that ANNs manage well. Considering only the inverse color intensity of the yellow channel, the calibration curve associated with this color change reaction is nonlinear and sigmoidal.

By training an ANN not only on this data, but also the three other color channels in the CMYK color space (cyan, magenta, and key), a more robust relationship between color change and associated glucose concentration may theoretically be developed.

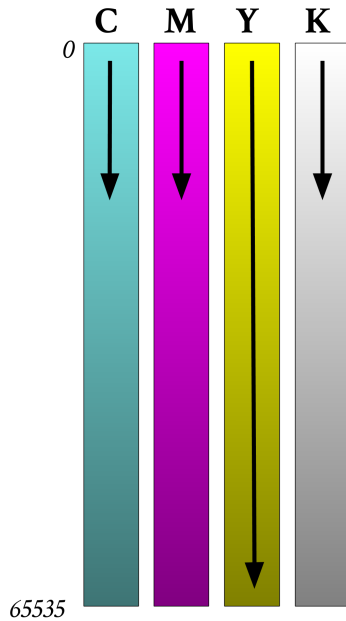


**Figure 3.5.** Most color change occurs along the yellow color channel in this reaction.

Secondly, unlike pH strip tests, where color variability is high when testing for acidity or basicity of a solution, this particular color change presents much more muted

variability. Glucose concentration color change is manifested colorimetrically primarily as a longitudinal change along one color [yellow] color channel as opposed to transverse across multiple color channels. In addition for it being difficult for users to visually interpret the results of the test, such a test also makes room for cross-entropy, meaning that close inputs yield very similar outputs.

Colorimetric analysis will be performed using ANNs that can provide a “best-guess” concentration value to an image of a colorimetric test strip based on a comprehensive database of sample images and corresponding concentration values.

This project was motivated by the need for immediate, electronic readout on colorimetric-based assays. Sending the color inputs through an ANN will enable the program to detect minute patterns and changes in variability unapparent to both the human eye and deterministic analytical approaches. This approach presents many advantages, one of which is high scalability. Once trained on a large enough dataset, ANNs may be implemented in code and distributed on mobile smartphone platforms. This is especially helpful when using the smartphone as an analytical device in resource-limited areas. The program can also be trained in real time, based on an ever-expanding dataset. The more the program is used the smarter it gets, and the lower the error rate. This platform will eventually get to a point where a patient would simply take a snapshot of a recently completed paper-based microfluidic assay. The smartphone would then be able to output the corresponding concentration. Achieving this would mean the overcoming of several obstacles, for instance, controlled lighting conditions—the

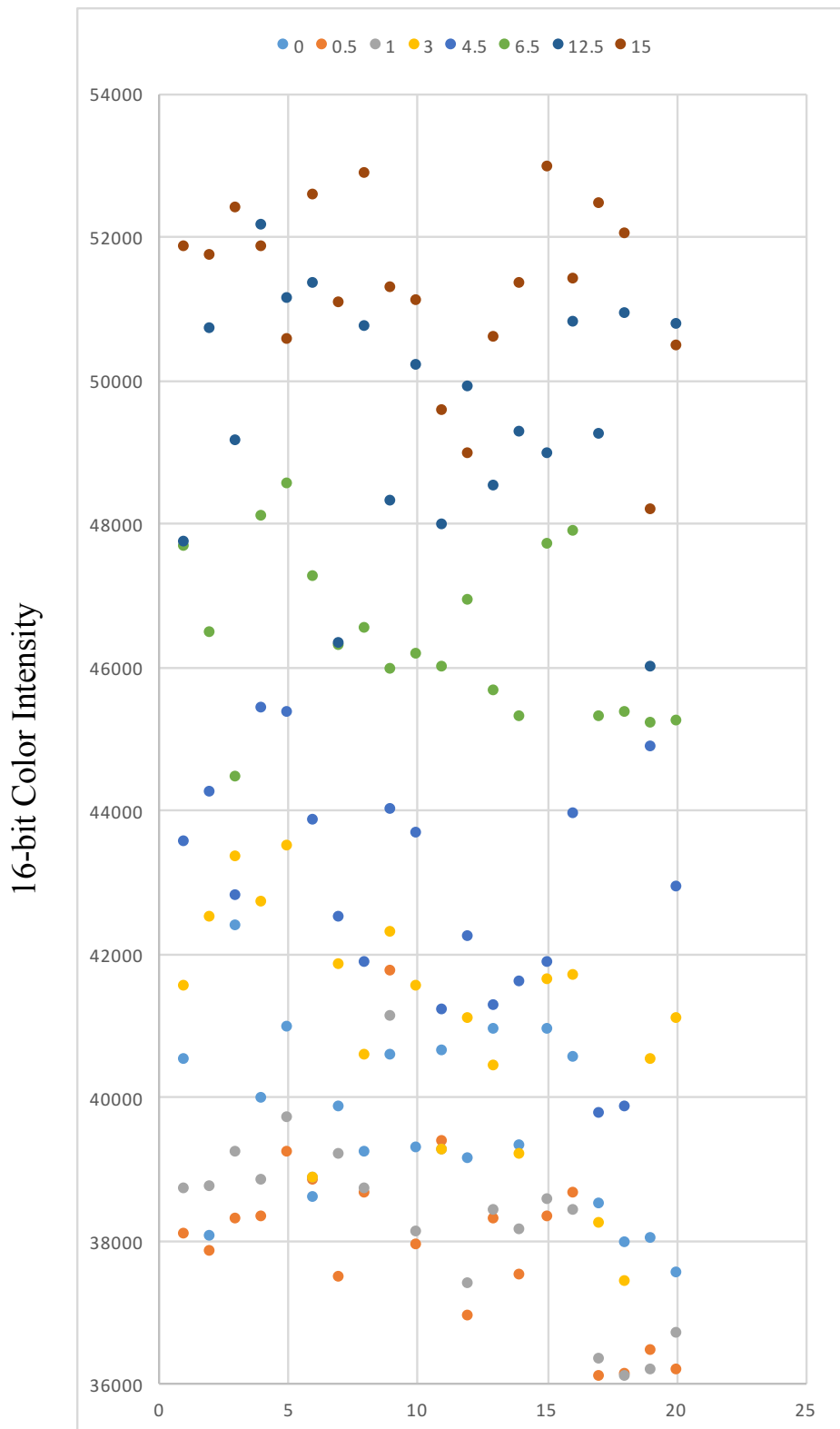


**Figure 3.6.** Scatter plot depicting cross entropy among concentration categories

slightest variation of which may influence the outcome. For the purposes of this research, a scanner is employed to provide controlled lighting. However, any step beyond this point would require additional algorithms to normalize lighting conditions. A method to mitigate varying lighting conditions is the “Experimental Methods” section.

### 3.1.4. Existing Work

*Léon, et al.* describe a method to evaluate food quality through colorimetric analysis [4]. The method described here makes use of MATLAB ANNs to facilitate a unit conversion from RGB to L\*a\*b color space. This methodology is mentioned here as a means by which a computer may autonomously use computer vision to extract relevant test areas from a chip. However, for the purposes of this research, this phase was skipped in favor of manual selection of test areas from scanned images. The ANN methodology used in this project is similar to that of *Zhang, et al.* to implement an artificial, colorimetric “nose” through a neural network-based pattern recognition (classification) algorithm to analyze concentrations of NH<sub>3</sub> [8]. This paper detailed two classification algorithms: linear discriminant analysis (LDA) and ANN, the former being a deterministic machine learning algorithm. A similar analysis was performed for this research. However, it was shown that ANN consistently produced higher positive identification rates than the deterministic models. Zhang’s methodology notably uses color change, *not* color, as its input vector. This idea was adopted in this research, as

using raw color values may render the neural network more susceptible to cross-entropy due to differing initial conditions across chips.

### 3.2. EXPERIMENTAL METHODS

#### 3.2.1. Normalizing Color and Lighting Conditions

To ensure properly controlled lighting conditions for colorimetric analysis, lighting conditions should first be normalized across samples. To achieve this, assay image acquisition should be performed with a color reference card, such as a true black or

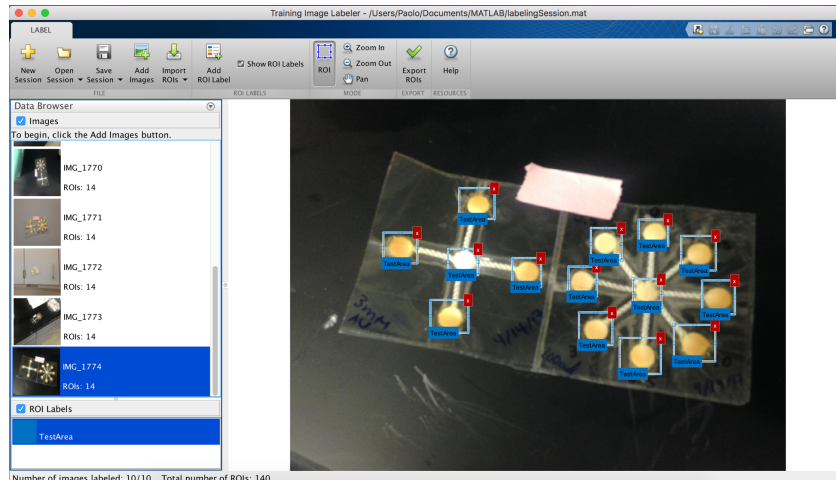


**Figure 3.7.** A manually labeled image of a microfluidic test strip/ array

18% gray middle reference card. This helps normalize nonstandard lighting conditions and set the white balance point of the analysis before introduction to the neural network. Dozens of tests will be conducted associating color variations and hues with concentration values. A picture will be taken of each assay. These photos will then be imported into the MATLAB Training Image Labeler app, where each test area on the

assay will be manually highlighted (Figure 3.7). Once a robust database of around one hundred labeled images has been built, the collected data may then be exported and used to train a neural network to identify test areas and automatically extract color data from the regions of interest. Colorimetric analysis may then be performed on each individual test area using the method described in *Léon, et al.* Alternatively, a document scanner with all computer-aided color correction features disabled works just as well. For this method, assays are scanned with a high quality scanner. The scans are then imported into Adobe Photoshop, where each region of interest is manually selected and color data extracted and averaged. This “brute-force” approach to color data extraction was used for this project.

### 3.2.2. Artificial Neural Network Training Methodology

Mean 16-bit color values from each of the four color channels in the CMYK histogram were extracted into an Excel spreadsheet using Adobe Photoshop. For each chip, the average CMYK color values from the 0 mM control test area were then subtracted from the other test areas each yielding four-component vectors of form  $\Delta\text{CMYK}_i = <\Delta C, \Delta M, \Delta Y, \Delta K>$  for each test area, where  $\Delta C = C_i - C_0$  and  $\Delta\text{CMYK}_0 = <0,0,0,0>$ . The spreadsheet used to train the neural networks consisted of 160 and 54 data points for the  $\mu\text{PAD}$  and  $\mu\text{TPAD}$ , respectively.

The artificial neural networks were implemented using the Neural Network Toolbox (v9.1) in MATLAB R2016b (v9.1.0.441655). For each of the two proposed chip

platforms (i.e.  $\mu$ TPAD and  $\mu$ PAD), two analyses were performed: fitting and classification. In all cases, seventy percent of the data points were allotted for a training sample, fifteen percent for a validation sample, and the remaining fifteen percent for an independent testing sample.

For fitting problems, the objective of the neural network is to predict a concentration value given a four-component input vector containing the test area CMYK color data. To achieve this, a two-layer feed-forward neural network with 30 hidden neurons (determined by trial and error to produce the most optimal results) was implemented in MATLAB and trained on an input matrix of size  $4 \times N$  (where  $N =$

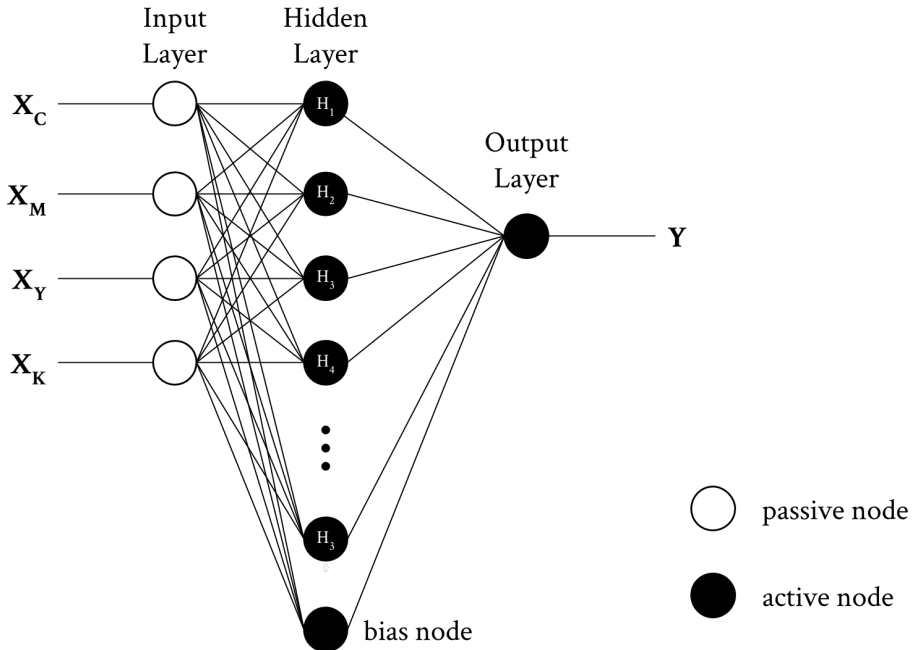


**Figure 3.8.** Neural network topology for regression

dataset size; 160 for  $\mu$ PAD, 54 for  $\mu$ TPAD) consisting of CMYK color data, and a target matrix of size  $1 \times N$  consisting of the corresponding known concentration values.

The topology of the fitting ANN (Figure 3.8) accepts a four component color vector of form  $\Delta\mathbf{CMYK}_i = <\Delta C, \Delta M, \Delta Y, \Delta K> = < X_C, X_Y, X_M, X_K >$  as input. The inputs were then passed on to four passive nodes acting as simple information buffers. Information then flows from the input layer to a hidden layer with a predetermined number of hidden neurons, 60 in this case. Each input node is connected to all neurons in the hidden layer.

Each hidden neuron, upon accepting inputs from the input layer, multiplies each input by a weight and adds a bias (usually of unity value) to the product. The sum is then sent through a sigmoidal activation function, as shown in Figure 3.9. In MATLAB, the sigmoidal function used is the hyperbolic tangent or  $tanh(x)$  function.

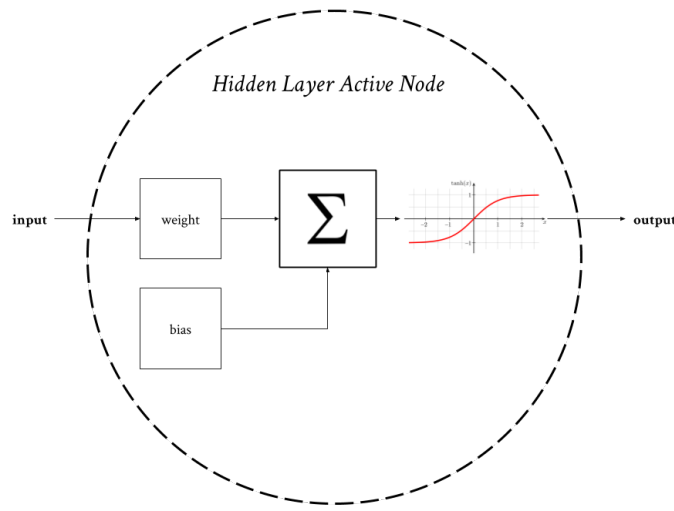


**Figure 3.9.** Internal block diagram for an active, hidden layer node

Each hidden layer neuron is connected to an output layer neuron. The size of the

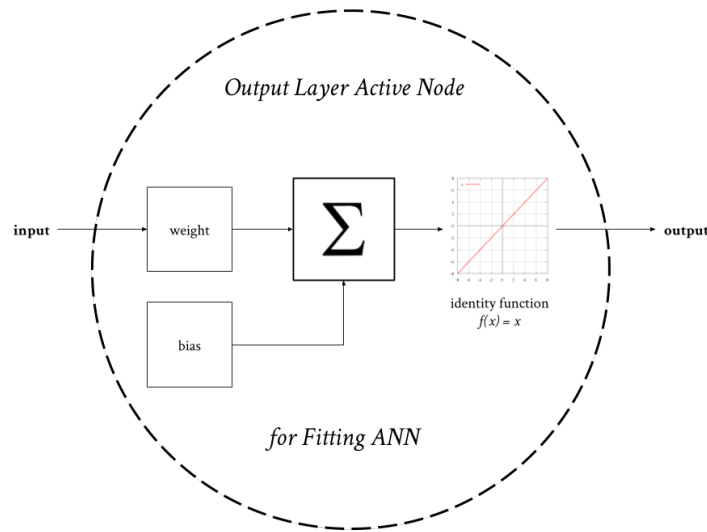


**Figure 3.10.** Internal block diagram for an active, output layer node in a linear regression problem

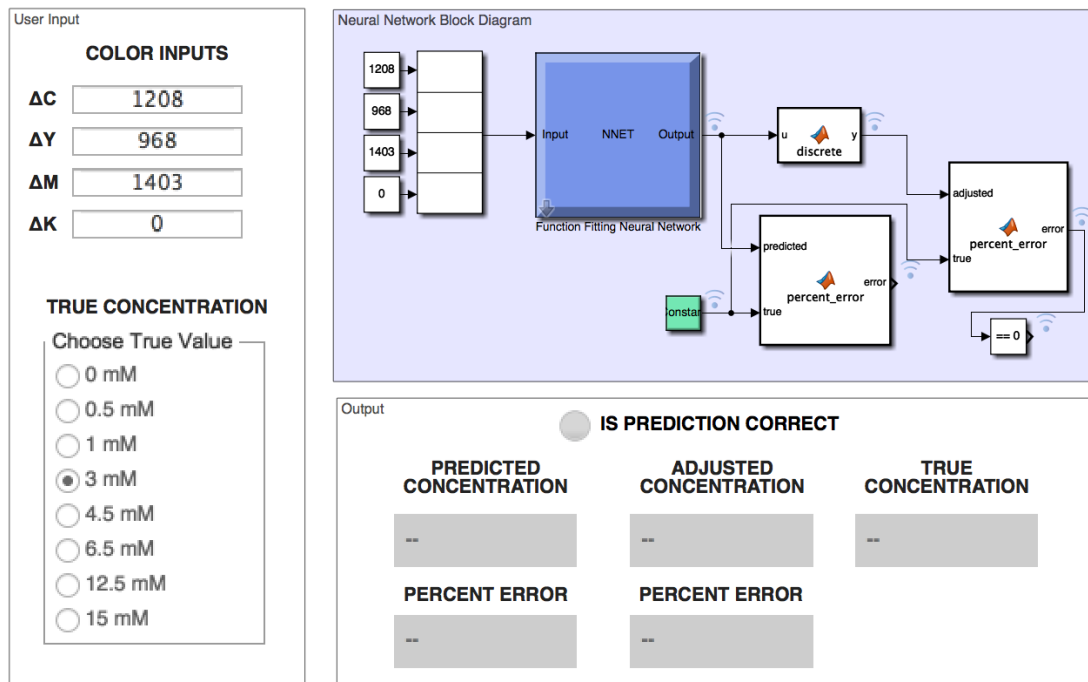
output layer is determined by the number of desired outputs. In this case only one output, concentration value, is desired. Each output layer neuron, like the hidden layer neurons, multiplies its inputs by a certain weight, adds a bias, and sends information through an activation function. For linear regression or fitting problems, the activation functions for each output layer active neuron is the identity function, as seen in Figure 3.10. The output of this neuron represents the concentration prediction of the ANN.

The neural network employed a Bayesian regularization backpropagation algorithm to train the network for 1000 epochs. Throughout training, the weights were dynamically adjusted to best fit the input data to the target data. After training, the solution was deployed as a block into Simulink 7.0. One disadvantage of the fitting algorithm for this application is that it was highly possible for the system to output

a value outside the set of known concentrations. For instance, the program may predict the concentration to be 12.38 mM instead of 12.5 mM. To restrict the output, the neural network block was placed in series with a custom MATLAB function block containing a script to discretize the output to the nearest known test strip concentration. For instance, raw outputs of 12.38 mM, 11.9 mM, and 13 mM were discretized to 12.5 mM. A custom graphical user interface (GUI) was developed in Simulink to output the raw prediction, its discretized (adjusted) value, and the percent error for each.

## NEURAL NETWORK-BASED REGRESSION PREDICTION PROGRAM for $\mu$ TPAD

Copyright © 2017 by Paolo Arguelles and the Research Lab of Dr. Frank A. Gomez



in affiliation with:



Department of Chemistry and Biochemistry

**Figure 3.11.** Custom Simulink GUI for fitting problem

The performance of the ANN fitting algorithm was quantified using the Pearson correlation coefficient (R), or R-value, which provides a measure of linear dependence between two variables. The correlation coefficient may assume any value between -1 and 1, inclusive. R-values of -1, 0, and 1 indicate perfect negative, independent, and positive correlations, respectively. This metric was used to provide a quantifiable measure of success for the Bayesian backpropagation algorithm used to train the ANN to predict glucose concentration based on color data.

The performance of ANNs applied to fitting problems such as this may be represented by scatter plots, shown in Figures 3.14A and 3.14B. Each data point on the plot indicates a prediction made by the ANN. The location of a data point along the horizontal axis labeled “Target” indicates the “true” glucose concentration of the analysis site, while the location along the vertical axis labeled “Output” indicates the glucose concentration guessed by the ANN. For an ANN with perfect predictive capability, the “Output” values equal the “Target” values, and all data points will reside on the “ $Y = T$ ” identity line, represented by the dotted line on the scatter plot. The Pearson correlation coefficient for a perfect ANN is  $R = 1$ .

For classification problems, the task of the neural network is to determine to which one of the following three arbitrarily defined classes a given test area belongs (**Class 1**: 0 mM, 0.5 mM, 1 mM; **Class 2**: 3 mM, 4.5 mM, 6.5 mM; **or Class 3**: 12.5 mM, 10 mM, 15 mM). To achieve this, a two-layer feed-forward neural network with sixty hidden neurons was implemented in MATLAB and trained on an input matrix of size  $4 \times$

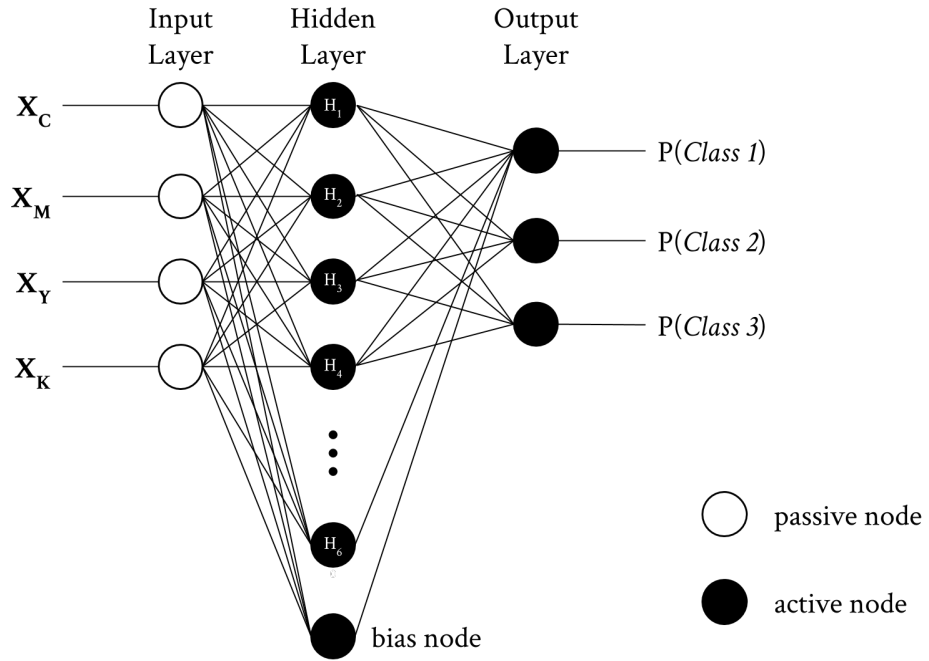


**Figure 3.12.** Neural network topology for classification

$N$  consisting of CMYK color data, and a binary target matrix of size  $3 \times N$  indicating the corresponding class.

The topology of a classifying ANN, shown in Figure 3.12, is identical to a fitting ANN, save for two main differences. First, each output neuron in a classifying ANN uses a softmax function as its activation function (Figure 3.3). The softmax function constrains each component of an output vector between 0 and 1, inclusive, and scales the values such that they produce a unity summation. For these reasons, the output of the softmax function may be seen as a probability distribution, an interpretation that is used for a classification ANN.

## NEURAL NETWORK-BASED CLASSIFICATION PREDICTION PROGRAM for $\mu$ TPAD

Copyright © 2017 by Paolo Arguelles and the Research Lab of Dr. Frank A. Gomez

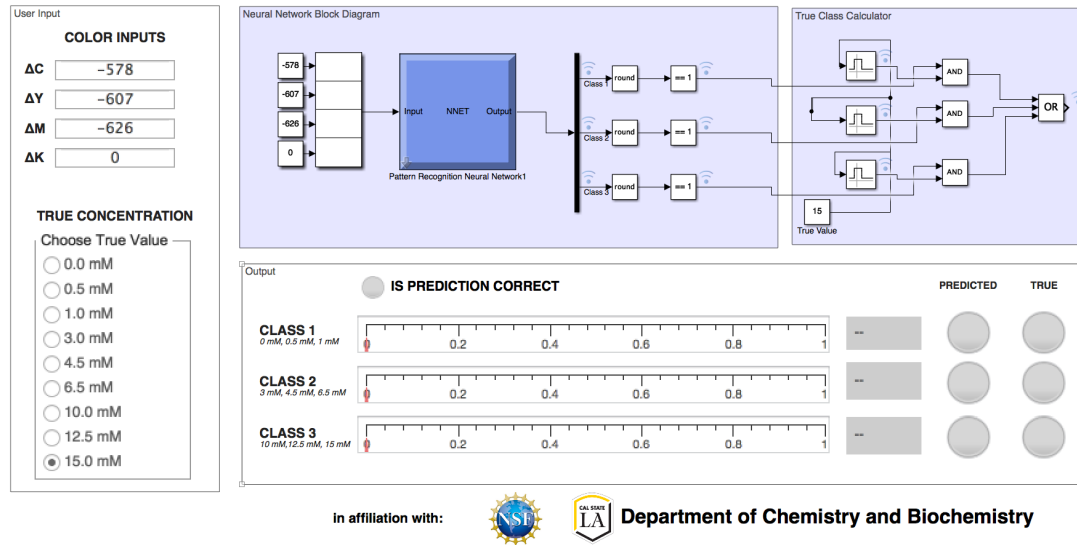


**Figure 3.13.** Custom Simulink GUI for classification problem

The choice of sixty hidden neurons in this ANN topology was arbitrary, and based on trial and error. The neural network employed a scaled conjugate gradient backpropagation algorithm to train the network for about twenty epochs. The solution was deployed as a block into Simulink 7.0 and implemented as a custom GUI. The GUI, shown in Figure 3.13, displays the calculated probability for each class given an input vector. The ANN prediction is taken to be whichever class yields the highest probability.

The performance of the ANN classification algorithm was expressed through confusion matrices, square tables with dimensions  $C \times C$  (where  $C$  is the number of possible classes into a dataset may be sorted) that represent the behavior of a classifier. For the  $3 \times 3$  confusion matrices shown in Figures 3.14C and 3.14D, the rows indicate the three “Output” classes into which the ANN may place an analysis site, where the

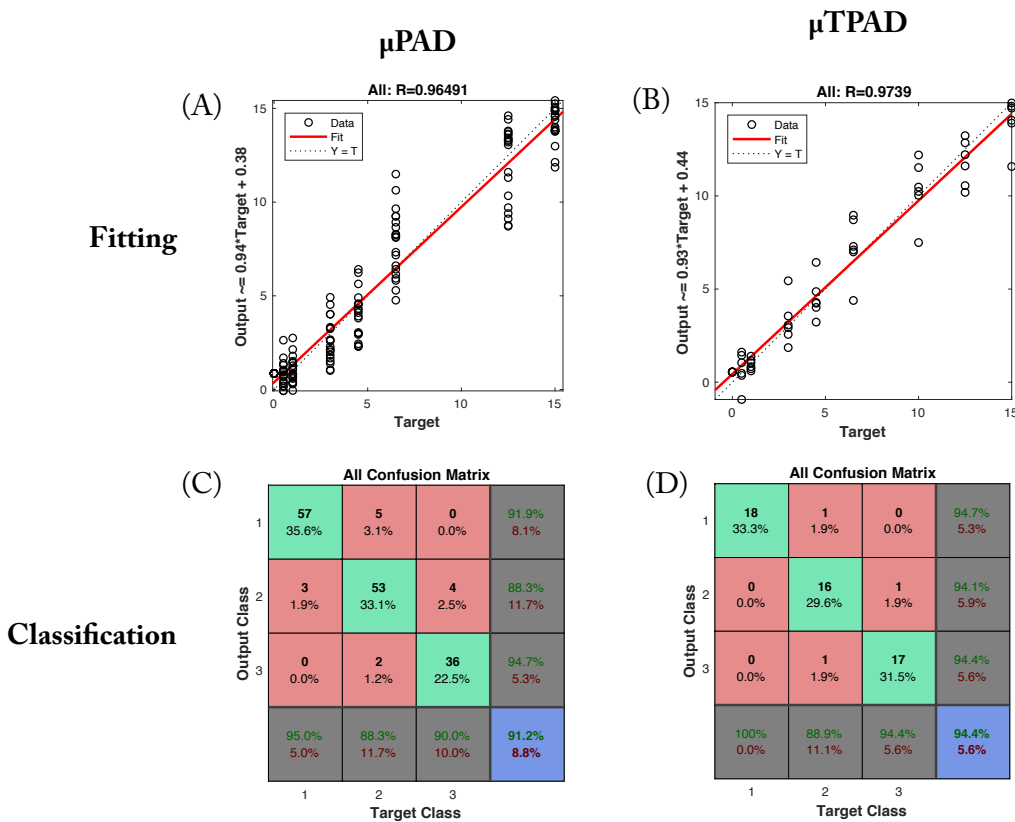


**Figure 3.14.** (A) Regression plot for μTPAD neural network fitting program, (C) Regression plot for μPAD neural network fitting program, (C) Confusion matrix for μTPAD neural network classification program, (D) Confusion matrix for μPAD neural network classification program

columns indicate the analysis site's corresponding true, or “Target” class. For instance, the “57” in the cell belonging to the first row and first column of the confusion matrix shown in Figure 3.14C indicates that the ANN classifier correctly classified 57 analysis sites belonging to Class 1 as Class 1 sites. The “3” in the cell belonging to the second row and first column of the confusion matrix in the same figure indicates that the ANN classifier misclassified three analysis sites belonging to Class 1 as Class 2 sites. The positive identification rate, or the ratio between number of samples correctly classified

and the number of total samples  $N$ , served as a metric to quantify the effectiveness of the classification algorithm.

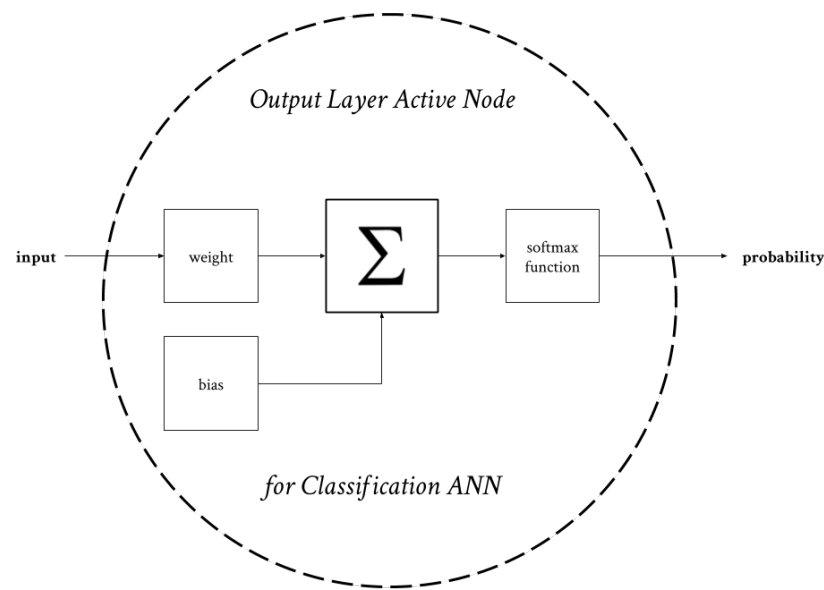


**Figure 3.15.** Internal block diagram of an active, output layer node in a classification problem

### 3.3. RESULTS AND DISCUSSION

The neural network-based prediction program proposed above has been proven to be effective, yielding positive classification rates in excess of 91% for classification problems (Figures 3.14C, 3.14D) and R-values in excess of 0.96 (Figures 3.14A, 3.14B; where 1 is perfect regression).

### *3.3.1. ANN Predictive Performance for μTPAD Platform*

An ANN was trained on the four-channel CMYK color data from 54 μTPAD analysis sites to evaluate the ability of fitting and classification machine learning algorithms to deduce glucose concentration for a thread- and paper-based microfluidic platform. Figure 3.14B shows the Pearson correlation coefficient to be  $R = 0.96491$ , indicating a highly linearly dependent relationship between the two variables, and excellent ANN fitting performance. The confusion matrix shown in Figure 3.14D indicates that the ANN correctly classified 94.4% (51 of 54 samples) of μTPAD analysis sites, indicating excellent ANN classification performance. The ANN was able to correctly identify all Class 1 analysis sites, and made no errors distinguishing between Class 1 and Class 3 sites. Three errors, each with one instance of occurrence (each accounting for 1.9% of the total number of classifications), were made: misclassifying a Class 2 site as a Class 1 site, a Class 3 site as a Class 2 site, and a Class 2 site as a Class 3 site.

As shown in Figure 3.14, for μTPAD, the performance of the ANN is approximated by the equation

$$\mathbf{Output}_T \approx 0.94\mathbf{Target}_T + 0.38$$

where  $\mathbf{Output}_T$  is the predicted concentration of the ANN, and  $\mathbf{Target}_T$  is the actual concentration. The “T” subscript indicates that this relationship is specific to the μTPAD

platform. To map the raw ANN outputs to the set of known  $\mu$ TPAD concentrations, the following operation is utilized

$$\text{Adjusted Output}_T = \text{Round}_{\text{TPAD}}(0.94\text{Target}_T + 0.38)$$

where function  $\text{Round}_{\text{TPAD}}$  is defined by

$$\text{Round}_{\text{TPAD}}(z) = \{C_T \in T \mid \min(C_T - z)\}$$

where  $z$  is a dummy variable representing the input of the function, and  $C_T$  is a member of set  $T = \{0, 0.5, 1, 3, 4.5, 6.5, 10, 12.5, 15\}$  containing all known concentrations (in mM) on the  $\mu$ TPAD platform.

### 3.3.2. ANN Predictive Performance for $\mu$ PAD Platform

An ANN was trained on the four-channel CMYK color data from 160  $\mu$ PAD analysis sites to evaluate the ability of fitting and classification machine learning algorithms to deduce glucose concentration for a 3D paper-based microfluidic platform. Figure 4A shows the Pearson correlation coefficient was  $R = 0.9739$ , indicating a highly linearly dependent relationship between the two variables, and excellent ANN performance. The confusion matrix shown in Figure 3.14C indicates that the ANN has correctly sorted 91.2% (146 of 160 samples) of the  $\mu$ PAD analysis sites. The errors the ANN was most likely to make were misclassifying a Class 2 site as a Class 1 site, which occurred in 3.1% (5 of 160 samples) of the data points, and misclassifying a Class 3 site as a Class 2 site, which occurred 2.5% (4 of 160 samples) of the data points. The ANN made no errors distinguishing between Class 1 and Class 3 sites.

As shown in Figure 3.14, for  $\mu$ PAD, the performance of the ANN is approximated by the equation

$$\mathbf{Output}_P \approx 0.93\mathbf{Target}_P + 0.44$$

where  $\mathbf{Output}_P$  is the predicted concentration of the ANN, and  $\mathbf{Target}_P$  is the actual concentration. The “P” subscript indicates that this relationship is specific to the  $\mu$ PAD platform. To map the ANN outputs to the set of known  $\mu$ PAD concentrations, the following operation is utilized

$$\mathbf{Adjusted\ Output}_P = \mathbf{Round}_{\mathbf{PAD}}(0.93\mathbf{Target}_P + 0.44)$$

where function  $Round_{PAD}$  is defined by

$$\mathbf{Round}_{\mathbf{PAD}}(z) = \{C_P \in P \mid \min(C_P - z)\}$$

where  $z$  is a dummy variable representing the input of the function, and  $C_P$  is a member of set  $P = \{0, 0.5, 1, 3, 4.5, 6.5, 12.5, 15\}$  containing all known concentrations (in mM) on the  $\mu$ PAD platform.

### 3.4. CONCLUDING REMARKS

The ability of a machine-learning approach to computationally interpret the results of thread/paper- and paper-based analytical devices has been demonstrated. Lapses in the ability of the ANN to form a representative and well-generalized relationship between four-channel CMYK data as system inputs and glucose concentration as system outputs may be attributable to the relative lack of color

variability in the observed color changes. This invariance results in high cross-entropy, limiting the pattern recognition capability of the ANN. However, a higher predictive resolution may be attained by chemically amplifying the color changes and training the ANN on a larger dataset. Of the two platforms analyzed, the  $\mu$ PAD is more practical for integration with ANN-based analytics due to its high degree of reproducibility and speed of production, allowing for large training datasets to be built in short periods of time.

In many ways, the fields of microfluidics and machine learning are complementary; inexpensive and highly reproducible analytical devices can provide the large datasets needed for ANNs to function well. The relative low cost and ease-of-reproducibility of the microfluidic devices described here combined with the high scalability of ANN-based algorithms through smartphone applications and other software deployment solutions make such a system ideal for rapid, POC diagnostics.

## REFERENCES

1. Agatonovic-Kustrin, S.; Beresford, R. *Journal of Pharmaceutical and Biomedical Analysis* 2000, 22 (5), 717–727.
2. Pal, S. K.; Mitra, S. *Fuzzy Sets and Systems* 1996, 80 (2), 121–132.
3. Widrow, B.; Lehr, M. *Proceedings of the IEEE* 1990, 78 (9), 1415–1442.
4. Agatonovic-Kustrin S., Beresford R., J. *Pharm. Biomed. Anal.* 2000, 22, 717–727.
5. Egmont-Petersen, M., de Ridder, D., Handels, H., *Pattern Recognit.* 2002, 35, 2279–2301.
6. Ali, H. S. M., Blagden, N., York, P., Amani, A., Brook, T. *Eur. J. Pharm. Sci.* 2009, 37, 514-522.
7. Peh, K. K., Lim, C. P., Quek, S. S., Khoh, K. H., *Pharm Res.* 2000, 17, 1384–1389.
8. Amani A, Mohammadyani D. Artificial neural networks: applications in nanotechnology. In: Hui C-L, editor. Artificial neural networks—application. Rijeka: INTECH; 2011.
9. Aghajani, M., Shahverdi, A. R., Amani, A., *AAPS PhamSciTech* 2012, 13, 1293-1301.
10. Esmaeilzadeh-Gharedaghi, E., Faramarzi, M. A., Amini, M. A., Najafabadi, A. R., Rezayat, S. M., Amani, A., *Pharm. Dev. Tech.* 2012, 17, 638-647.
11. Orimoto, Y., Watanabe, K., Yamashita, K., Uehara, M., Nakamura, H., Furuya, T., Maeda, H. J., *Phys. Chem. C.* 2012, 116, 17885-17896.
12. Fakhrabadi, M. M. S., Samadzadeh, M., Rastgoo, A., Yazdi, M. H., Mashhadi, M. M., *Physica E: Low Dimens. Syst. Nanostruct.* 2011, 44, 565-578.
13. Ahadian, S., Mizuseki, H., Kawazoe, Y., *Microfluid. Nanofluidics* 2010, 9, 319-328.
14. Lee, D. S., Jeon, B. G., Ihm, C., Park, J. K., Jung, M. Y., *Lab Chip* 2011, 11, 120–126.

15. Nash, M. A., Hoffman, J. M., Stevens, D. Y., Hoffman, A. S., Stayton, P. S., Yager, P., *Lab Chip* 2010, 10, 2279–2282.

## CHAPTER 4.

### PASSIVE LOGIC ON PAPER MICROFLUIDICS

#### 4.1. INTRODUCTION

The half-adder circuit forms the basis of all computational ability in a computer. The circuit is able to add together two 1-digit binary numbers (with no carry-in) and produce a sum bit  $S$  and carry-out bit  $C_{out}$ . Half and full adders have been implemented using a variety of media (e.g. Legos, K'nex, pinballs, string, etc.), most notably by stand-up mathematician Matt Parker on the YouTube channel *Numberphile*, where a four-bit



**Figure 4.1.** A four-bit domino adder

adder was demonstrated using dominoes in strategically placed configurations (Figure

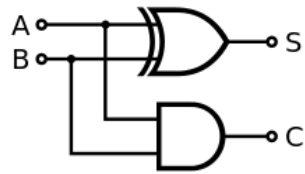


**Figure 4.2.** Circuit diagram for a conventional half-adder

4.1). Implementing any kind of complex logic in a paper-based microfluidic medium, however, is largely unprecedented.

The main advantage of microfluidic paper-based logic circuits is its passivity.

$C_{out}$	S	in <sub>1</sub>	in <sub>0</sub>
0	0	0	0
0	1	0	1
0	1	1	0
1	0	1	1

**Figure 4.3.** Behavior for a half-adder

Conventional logic circuits rely on an active flow of electrons. Even in microfluidics, many logic gates rely on active fluidic pumps for proper operation. However, passive circuits will allow logical operations to be performed without the need for an external electromotive force; such a circuit relies only on the intrinsic capillary properties of paper.

A half adder may be implemented structurally with circuits using an XOR gate and an AND gate (Figure 4.2).

There is literature describing the implementation of AND gates in microfluidics, but hardly any for implementing XOR gates using this platform. Furthermore, as previously noted, there is hardly any precedent for implementing logic gates, let alone half adders, on paper microfluidics. Channel size and capillary action also need to be taken into account, meaning that a half adder may not be implemented passively using the above design, as the paper substrate will likely run out of “fuel” before it could complete the operation. The adder must, therefore, be implemented functionally, not structurally, and be designed according to the behavior of the truth table in Figure 4.3.

Literature on implementing logic gates and half-adders in microfluidics is sparse, let alone implementation on paper microfluidic platforms. *Cheow, et al.* present a method for implementing two-input AND/OR gates and one-input NOT gates on polydimethylsiloxane (PDMS) substrate by varying channel width [3]. *Prakash and Gershenfeld* present a similar method, demonstrating the implementation of AND/OR/NOT gates, toggle flip-flop, and ripple counter using “bubble logic,” or the strategic introduction of bubbles into PDMS microchannels to achieve such logical behavior [5]. This, however, relies on the periodic introduction of signal bubbles using an active pump, something that would not be feasible in a paper substrate. Once again using PDMS substrate, *Vestad and Mar* demonstrate that any Boolean operation may be realized microfluidically if there exists method to vary the flow resistance within that substrate [6]. The paper notes that these basic Boolean functions “can be combined to form more complicated devices such as a half adder.” A novel method to implement a half-adder on

a microfluidic chip is demonstrated by *Wang and Huang* [7]. This novel method makes use of bioreactions, utilizing “a DNA strand as an operand.” The project detailed in this chapter posits that a binary half adder may be realized through much simpler means, using basic acid-base chemistry.

## 4.2. EXPERIMENTAL METHODS

### 4.2.1. Phenolphthalein as an Indicator of Basicity

Phenolphthalein owes its indicative nature to the Brønsted-Lowry model of acid-base reactions. Because phenolphthalein is a weak acid, it tends to donate its hydronium cations ( $H^+$ ) to bases. When stripped of its hydronium cation, phenolphthalein assumes a

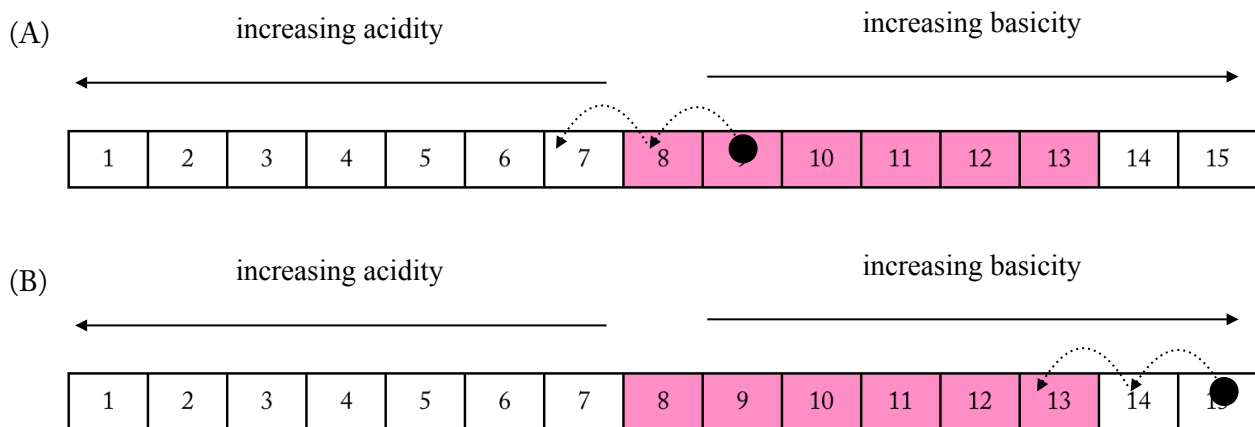


**Figure 4.4.** (A) The dynamics of the “S” test area (not to scale), (B) the dynamics of the “C” test area (not to scale)

pinkish hue. By simply observing the hue of the solution, one could easily determine the relative basicity of the overall solution. By breaching the pH threshold at which

phenolphthalein turns pink, this indicative property may be exploited to design a binary half adder on a passive microfluidic platform.

#### *4.2.2. Implementing the Half-Adder*

In the paper microfluidic design of the half adder, logic-0 and logic-1 are defined at the input as whether or not a solution is spotted onto the corresponding sample area, and at the output as either the absence or presence of color, respectively. A design must be introduced such that the “S” test area turns colored when only one input is spotted, but turns colorless when both inputs are spotted. Conversely, the “C” test area should turn colored only if both inputs are spotted. This may be achieved by letting the input solution be an equal parts cocktail of phenolphthalein indicator and weak acid (vinegar, 4% acetic acid), and presetting basic solutions onto the output areas. Knowing that phenolphthalein assumes a pinkish hue between a pH of around 8.2 to 13.0, the paper-based half adder will act, in theory, as follows.

The black dot in Figure 4.3A represents the initial concentration of the “S” test area. Each “jump” represents one aliquot of solution being added to the system. One jump depicts the (0,1) and (1,0) cases, while two jumps depicts the (1,1) case. The pink shaded area represents the indication region of phenolphthalein (keep in mind that the test area will not actually turn colored unless the input solution containing phenolphthalein is added to the system). Note that, for the “S” test area, the addition of one aliquot of solution will make the test area colored, while the addition of two aliquots will make the

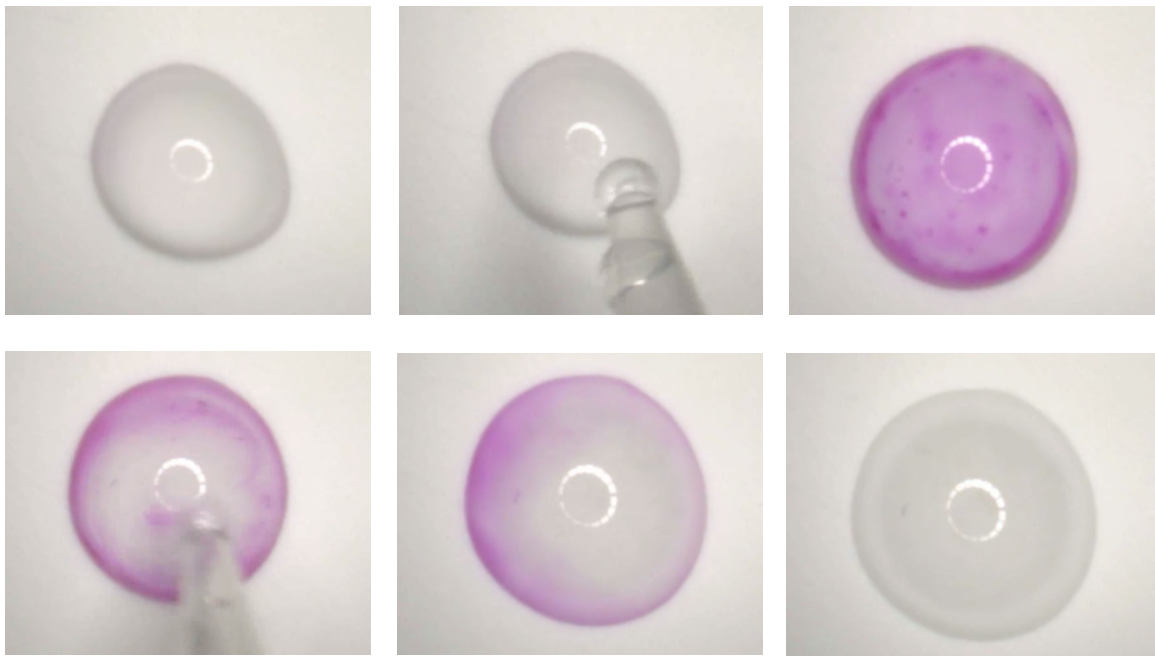


**Figure 4.5.** A  $1.0 \mu\text{L}$  solution of  $13.5 \text{ NaOH}$  acts as the pre-spotted output “S” area (*top left*), one aliquot of  $0.5 \mu\text{L}$  of equal parts phenolphthalein and vinegar is added to the solution (*top middle*), producing color (*top right*). Another aliquot of input solution is added to the colored mixture (*bottom left*), producing a colorless mixture (*bottom middle, right*).

test area clear. For the “S” test area, the addition of one aliquot of solution will render no color change in the test area, while the addition of two aliquots will make the test area colored. Before experimenting with paper substrate, tests were performed on a hydrophobic surface to create an ideal mixing scenario.

#### 4.3 RESULTS AND DISCUSSION (PRELIMINARY)

It was found, for ideal mixing, that  $0.5 \mu\text{L}$  aliquots of input solution and a pre-spotted  $1.0 \mu\text{L}$  basic solution (NaOH with pH 13.5 for “S”) will realize the dynamics above (Figure 3.4). It is still unclear what the initial concentration of “C” would need to

be, although it is presumed that [C] will need to be a very strong base. Furthermore, all tests were conducted under ideal mixing conditions; it is unclear what substantial effect realizing this design on paper substrate will be, given non-homogeneous capillary mixing.

#### 4.4 CONCLUDING REMARKS

The paper-based half adder design proposed here is subject to the following limitations. Firstly, the half-adder design proposed here is both single-use and single-stage. This design cannot be reused due to its implementation on a passive paper medium, due to the inability to “clean” or “reset” the device once a solution propagates throughout the medium. The design cannot be used modularly, as some color due to phenolphthalein indicator propagation will present itself in succeeding stages, regardless of whether or not that stage is meant to produce that output. For example, if a stage one half adder produces a colored output, that colored output will propagate to a second stage half adder that is attached at its input to the output of the first. Unless there exists a chemical mechanism to control this unwanted propagation, a cascade design using multistage half adders of this type to realize more complex operations is infeasible. While the design proposed here is the first of its kind to be implemented on paper substrate, there is clearly more work to be done before a passive paper-based analytical device of meaningful, substantial computing capability can be realized on this platform.

## REFERENCES

1. Burks, T. F.; Shearer, S. A.; Gates, R. S.; Donohue, K. D. *Transactions of the ASAE* 2000, 43 (4), 1029–1037.
2. Chang, B.-Y.; Crooks, J. A.; Chow, K.-F.; Mavré, F.; Crooks, R. M. *Journal of the American Chemical Society* 2010, 132 (43), 15404–15409.
3. Cheow, L. F.; Yobas, L.; Kwong, D.-L. *Applied Physics Letters* 2007, 90 (5), 054107.
4. León, K.; Mery, D.; Pedreschi, F.; León, J. *Food Research International* 2006, 39 (10), 1084–1091.
5. Prakash, M.; Gershenfeld, N. *Science* 2007, 315 (5813), 832–835.
6. Vestad, T.; Marr, D. W. M.; Munakata, T. *Applied Physics Letters* 2004, 84 (25), 5074–5075.
7. Wang, J.; Huang, Y. *IEEE Transactions on NanoBioscience* 2014, 13 (2), 146–151.
8. Zhang, Y.; Luo, X.-G.; He, K.; Huo, D.-Q.; Liu, J.; Liu, P.; Shi, X.-J.; Hou, C.-J. *Water, Air, & Soil Pollution* 2012, 223 (6), 2969–2977.

# CHAPTER 5.

## DIGITAL MICROFLUIDIC PAPER ANALYTICAL DEVICES

### 5.1. INTRODUCTION

Conventional microfluidic paper analytical devices ( $\mu$ PADs) rely on the intrinsic capillary properties of the paper to achieve passive flow through pre-defined channels. The capabilities of such devices can be elevated through digital microfluidics (DMF).

#### 5.1.1. *The Electrowetting-on-Dielectric Phenomenon in DMF Devices*

The ability to control the affinity of a water droplet to a surface results in controlled droplet actuation for implementation in DMF devices. This chapter will address the mechanics of EWOD devices, droplet actuation on conventional PCB and paper substrates, and how the four droplet operations may be achieved through the use of a microcontroller.

Applying a high voltage to a droplet of water on a hydrophobic surface changes the affinity of the water to that surface, enabling on-demand toggling between hydrophobic and hydrophilic behavior. This phenomenon is called electrowetting-on-dielectric (EWOD), and is the theory upon which most DMF devices operate. When EWOD is applied to an electrode array, the individual regions above each electrode may be programmed to act as a hydrophobic surface or hydrophilic surface. Activating

adjacent electrodes in quick succession can result in the digital relocation of the droplet over the array.

When no voltage potential is applied, the water droplet obeys the hydrophobic properties of the layer upon which it sits, and sits with contact angle greater than 90 degrees. The contact angle, defined as the smallest angle between the surface vector of the plane upon which the droplet is sitting and the tangential vector to the interface of the droplet and hydrophobic surfaces, serves as a measure of hydrophobicity for a given material.

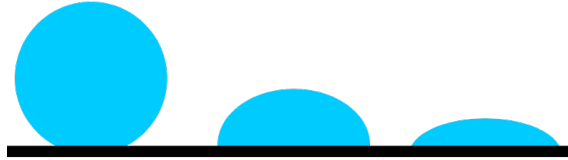


**Figure 5.1.** Water droplets with contact angles of (left)  $120^\circ$ , (middle)  $90^\circ$ , and (right)  $50^\circ$

Generally speaking, a contact angle less than  $90^\circ$  is an indicator of hydrophilicity, while a contact angle greater than  $90^\circ$  is an indicator of hydrophobicity. When a positive, non-zero potential is introduced, a capacitance  $C$  is generated within the dielectric layer, causing the water droplet to act hydrophilic. The magnitude of this capacitance is given by

$$C = \frac{\epsilon A}{t} \quad (4.1)$$

where  $\epsilon$  is the absolute permittivity of the dielectric layer,  $A$  is the area of overlap between the two plates in square meters, and  $t$  is the thickness of the dielectric layer in

meters. The application of a high electric potential yields an excess of free energy at the interface of the water droplet and the dielectric layer. The system will tend to minimize this free energy by maximizing capacitance  $C$ . Since  $t$  and  $\epsilon$  are constant, the system will resort to maximizing  $A$ , the area of overlap between the electrode and the water droplet, by moving the droplet above the center of the activated electrode. Opposite charges will align on either side of the dielectric layer, causing the droplet to spread and fill the region above the activated electrode.

### 5.1.2. Electrowetting Theory

A theoretical analysis into the electrowetting phenomenon requires an examination of the forces at play in a three-phase environment, where liquid, gas, and solid meet. Mathematically, the phenomenon may be described in terms of thermodynamics. The total surface tension  $\gamma_{ds}$  between the water droplet and hydrophobic surface can be expressed as the summation of mechanical and electrical components by

$$\gamma_{ds} = \gamma_{mechanical} + \gamma_{electrical} = \gamma_{ds}^0 - \frac{CV^2}{2} \quad (5.2)$$

where  $\gamma_{ds}^0$  is the total surface tension between the water droplet and hydrophobic surface at zero applied potential,  $C$  is the capacitance of the dielectric layer, and  $V$  is the applied potential. Consider the Young-Dupré relation describing the interfacial energies of a triphasic boundary region:

$$\gamma_{sg} - \gamma_{sl} = \gamma_{lg} \cos \theta \quad (5.3)$$

where, for a region at which solid, liquid, and gas meet,  $\gamma_{sg}$  is the interfacial surface tension between solid and gas,  $\gamma_{sl}$  is the interfacial surface tension between solid and liquid,  $\gamma_{lg}$  is the interfacial surface tension between liquid and gas, and  $\theta$  is the contact angle.

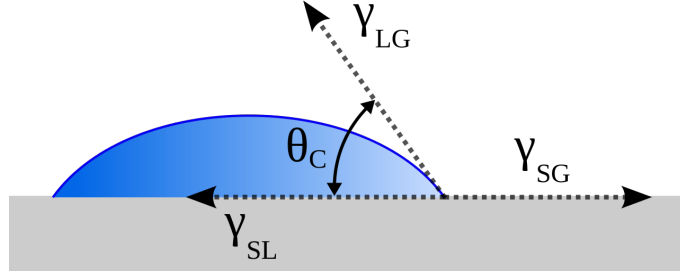


**Figure 5.2.** The triphasic boundary in the electrowetting model showing relevant quantities

angle. A graphical representation of the quantities involved in the Young-Dupré relation is shown in Figure 5.2. Rewriting this trivial relationship to the EWOD model:

$$\gamma_{ds} = \gamma_d - \gamma_s \cos \theta \quad (5.4)$$

where  $\theta$  is the contact angle,  $\gamma_d$  is the interfacial surface tension between the water droplet and the ambient environment, and  $\gamma_s$  is the interfacial surface tension between the hydrophobic surface and ambient environment. Using Equations (5.2) and (5.4), an equivalency can be drawn:

$$\gamma_{ds}^0 - \frac{CV^2}{2} = \gamma_d - \gamma_s \cos \theta. \quad (5.5)$$

Redistributing, the contact angle  $\theta$  may be expressed in terms of voltage:

$$\theta = \cos^{-1} \left( \frac{\gamma_s - \gamma_{ds}^0 + \frac{CV^2}{2}}{\gamma_d} \right) \quad (5.6)$$

leading to the trivial conclusion that the higher the voltage, the more wettable the surface, and the lower the contact angle. In short, the higher the voltage, the more hydrophilic the surface behaves.

### 5.1.3. Contact Angle Saturation

While true for the purposes of an EWOD device, the conclusion is subject to a caveat: contact angle droplet actuation velocity is limited by contact angle [10]. As shown in Figure 5.3, regardless of applied voltage, the velocity of an actuated droplet asymptotically approaches the point at which its contact angle is 180 degrees, resulting in contact angle saturation [11]. If velocity control is desired, the surface should be treated with enough hydrophobic coating such that the contact angle resides within the greyed region labeled in Figure 5.3 as “most effective area.”

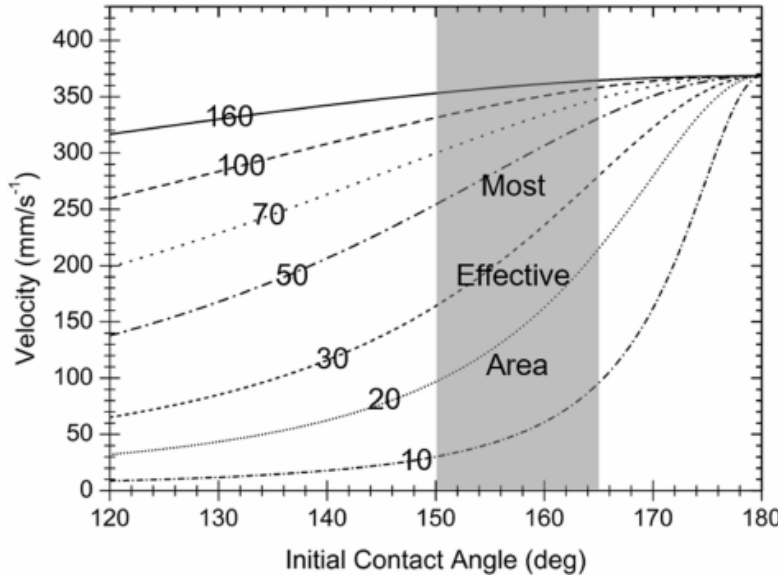


**Figure 5.3.** Saturation velocity vs. contact angle curves, controlled by applied actuation voltage

#### 5.1.4. *Droplet Operation Types*

The successful demonstration of smooth droplet actuation on a properly prepared hydrophobic surface will allow the realization of four different analytical fluidic operations:

1. Transport - *moving a droplet from one place to another*
2. Creation - *creating droplets of a prescribed volume from a reservoir*
3. Splitting - *splitting a droplet into two aliquots of equal volume*
4. Merging - *merging two droplets into one*



**Figure 5.4.** An EWOD device in *sandwich* (left) and *open-faced* (right) configurations

#### 5.1.5. *DMF Device Configurations*

DMF devices are traditionally designed in either an open-faced (Figure 5.4B) or sandwiched (Figure 5.4A) configuration. The two device configurations are identical, save for the addition of a ground electrode on the sandwich design. In both setups, the droplet scurries on top of a thin hydrophobic layer on an array of controlled, high voltage electrodes. In the sandwich configuration, a hydrophobic indium tin oxide- (ITO) coated glass acts as a ground electrode.

### *5.1.6. The D $\mu$ PAD*

In this chapter, a digital microfluidic paper analytical device (D $\mu$ PAD), a novel platform merging paper and digital microfluidics, is proposed. A microfluidic paper analytical device enriched with DMF capabilities will enable:

1. the realization different topologies for the design of paper microfluidic devices
2. precise multiplexing and volume deposition of droplets
3. higher speeds for the analysis process for paper microfluidic platforms
4. management of time-sensitive reactions

## **5.2. EXPERIMENTAL METHODS**

For the sake of simplicity, the open-faced design (Figure 4.3B) was used for this project. The fabrication process consisted of two parts: creating the electrode array and the hydrophobic dielectric layer.

### *5.2.1. Creating the Electrode Array*

#### **Photolithographic PCB Etching**

The electrode array over which the droplets would travel was created using the photolithography circuit board fabrication method. This PCB etching method requires access to presensitized positive photoresist printed circuit boards (PCBs), 1% sodium hydroxide (NaOH) as developer solution, acetone, deionized water, and a ferric chloride (FeCl) copper etching solution. A transparent mask of the desired electrode layout was

first created on Inkscape. The design was then printed onto transparent film with black ink using a conventional, high quality inkjet printer.

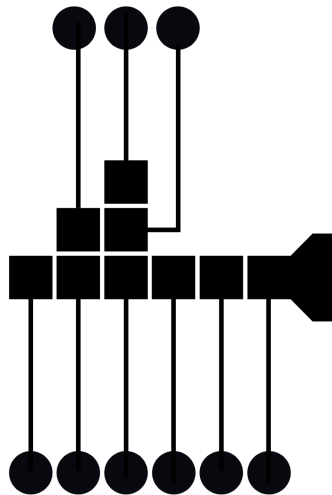


**Figure 5.5.** The transparent mask used for PCB photoresist etching

In a dark room, the protective covering on the photoresist layer was removed, and the transparent mask carefully placed onto the exposed area. A glass microscope slide was placed on top of the transparent film to ensure every part of the transparent mask was in contact with the presensitized area. The unit was exposed to a white single-watt lightbulb for seconds. The exposure process may be streamlined by using an ultraviolet (UV) flashlight instead of a bright light. If a UV light is used, the exposure time should be limited to no more than 30 seconds. Alternatively, computer paper may be used as the mask with an exposure time of 5 minutes; any longer, and the chip will become overexposed, and the design corrupted. Figure 5.6 details the photolithography exposure process.

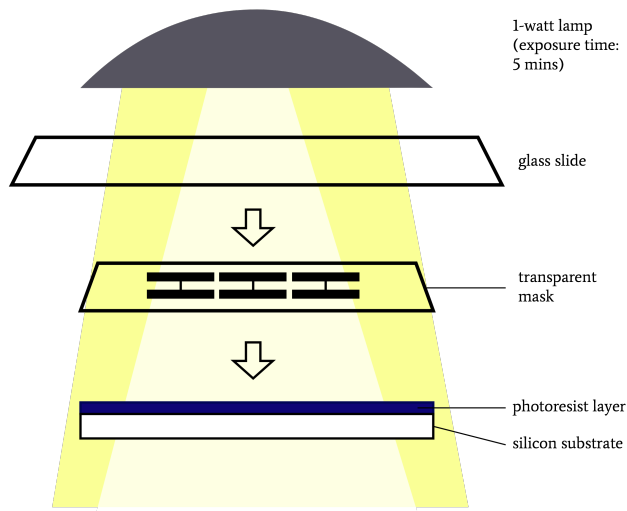


**Figure 5.6.** Configuration of the presensitized PCB, transparent mask, and glass slide during the exposure step of the photolithography process

The PCB was then placed in a glass dish containing the sodium hydroxide developer solution, and was continuously perturbed until a clear pattern matching the

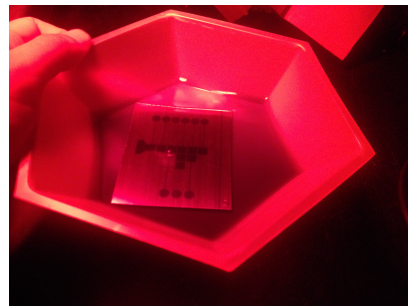


**Figure 5.7.** The exposed PCB is developed via sodium hydroxide ( $\text{NaOH}$ ) immersion

mask appeared on the PCB surface. The PCB was then rinsed with deionized water, and placed in another dish containing ferric chloride copper etching solution, where it was continuously perturbed for 30 minutes to facilitate the etching process. Throughout



**Figure 5.8.** The photosensitized PCB is immersed in ferric chloride etching solution.

etching, the PCB board was checked periodically to ensure that all copper is removed, except that under the regions of the board still obscured by the photoresist layer. Once all copper has been removed, the PCB was rinsed with deionized water, and swabbed with acetone to remove the remaining photoresist. The completed PCB should be rinsed, polished, and dried as needed.

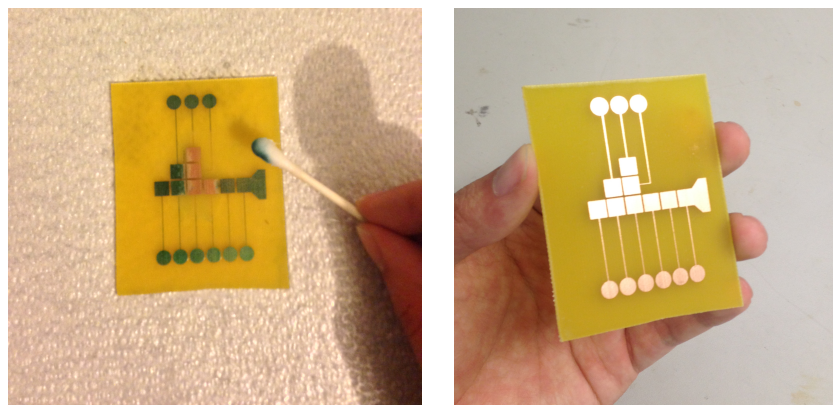


**Figure 5.9.** Acetone is swabbed on the etched board to remove the remaining photoresist film and complete the photolithography process.

## **Third Party PCB Etching**

For DMF applications requiring the highly precise manipulation of nanofluidic aliquots, photolithography is not an ideal PCB milling method. Sufficiently narrow electrode pad spacing is essential to the performance of the DMF chip. Inkjet printers, even high quality ones, may not be able to provide the level of resolution needed to print transparent masks with narrow electrode spacing. PCBs were designed on EAGLE, and sent to a third-party PCB miller such as OSHPark for professional etching.

### *5.2.2. Creating the Hydrophobic Dielectric Layer*

#### **Using Rain-X**

A hydrophobic layer may be achieved via commercial, off the shelf (COTS) hydrophobic auto spray. Parafilm M PM999 All-Purpose Laboratory Film was soaked in Rain-X, a commercially available water repellent spray, for 20 minutes. Silicone oil was then spread on the PCB containing the electrode array to maximize contact with the Parafilm and minimize unwanted air bubbles. The soaked Parafilm was then stretched over the PCB. A Q-tip cotton swab was used as a miniature roller to remove any trapped air bubbles between the film and the PCB. A heat gun was used to cure the hydrophobic spray onto the film, and the film onto the PCB.

## **Using FluoroPel PFC1601V**

For more professional applications, FluoroPel, a hydrophobic and oleophobic coating from Cytonix, may be spin coated onto a thin glass surface to render it superhydrophobic. Parafilm and glass were placed into an ultrasonic bath containing water, isopropanol, and salt for 15 minutes. The glass was then placed in an 80°C oven to dry. The film was then placed onto a spin coater. 150 to 200  $\mu\text{L}$  of FluoroPel (8cm x 4cm) was applied to the glass, and spun for 30 seconds at 3000 RPM. The spin-coated glass was left to cure on a hot plate at 80°C for 20 minutes, then at 150°C for 30 minutes. The glass was then left to dry before use.

### *5.2.3. Designing the Electrode Array Circuitry*

Each electrode pad is connected to a power MOSFET (BSP89) to toggle a 200 VDC connection. This MOSFET model was chosen because of its logic-level rating up to voltages of 240 VDC, well beyond the 200 VDC found to actuate droplets. Additionally, their “logic-level” designation allows each transistor to be toggled via a 5V logic line from an Arduino, or other commercial microcontroller. Each MOSFET is connected in an “active-low” configuration, in series with a 180  $\text{k}\Omega$  pull-up resistor. A logic-0 (low) level sent by the microcontroller yields a 200 VDC potential at the electrode pad, while a logic-1 (high) level corresponds to a 0 VDC potential.

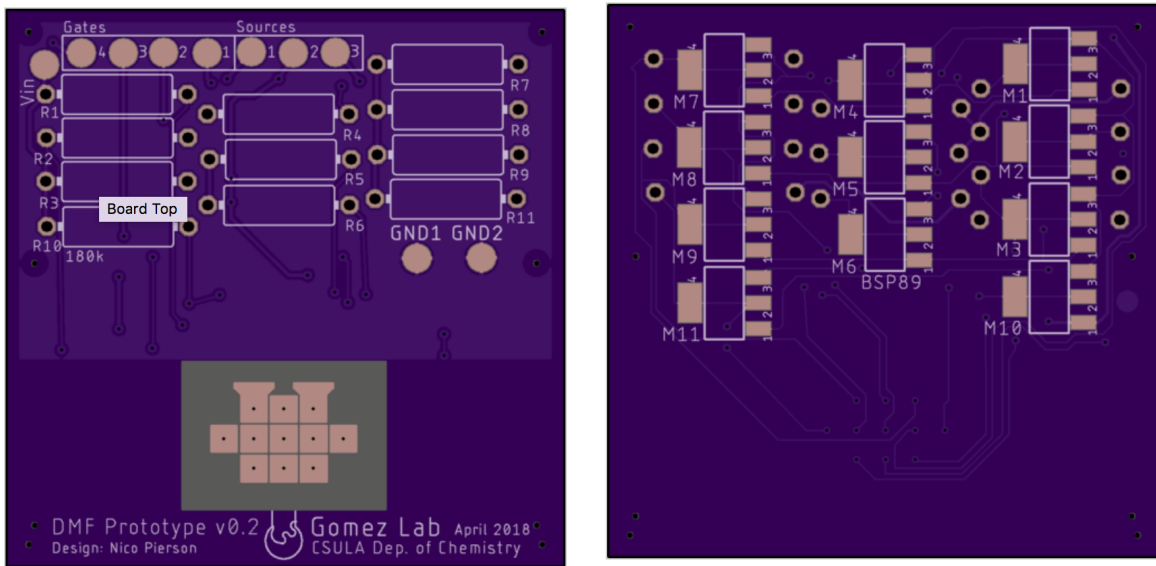


**Figure 5.10.** Custom PCB for DMF electrode array. (*Design by Nico Pierson*)

### 5.3 RESULTS AND DISCUSSION (PRELIMINARY)

The minimum voltage to achieve droplet actuation was found to be 200 VDC. It should be noted that this droplet actuation voltage is specific to the preparation method of the hydrophobic coating detailed above. The voltage may conceivably be decreased to levels as low as 11 VDC, given professional hydrophobic treatment [8, 9]. Simple droplet translation using a 200 VDC actuation voltage was observed using this topology. For more complex operations involving droplet splitting, an interleaved jagged electrode design should be adopted.

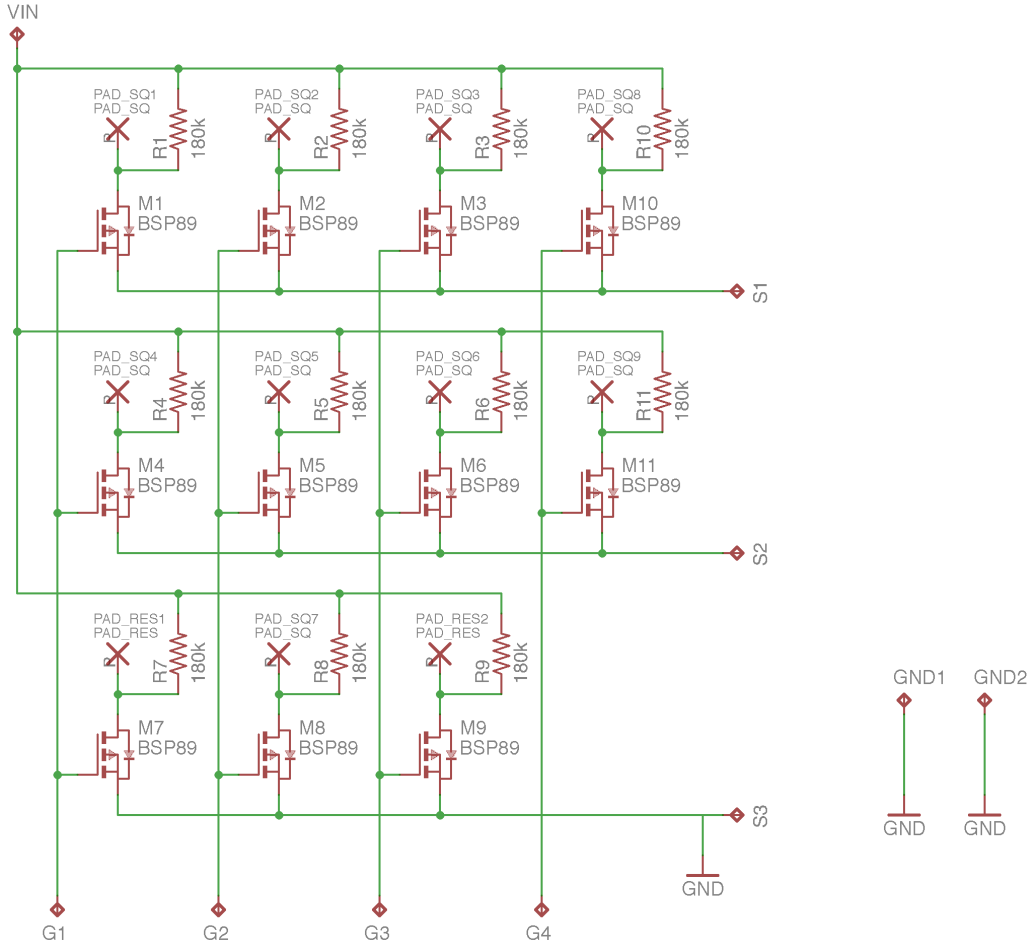


**Figure 5.11.** Circuit schematic of a DMF electrode array. Design by Nico Pierson.

## 5.4 CONCLUDING REMARKS

### 5.4.1. DMF-Enabled ELISA Microsystem

One of the potential applications of this technology of particular interest to analytical chemists is its potential integration with an enzyme-linked immunosorbent assay (ELISA) [1-7]. Electrodes can be embedded into the channels of a passive paper-based ELISA to speed up time sensitive reactions, and facilitate accurate volume deposition. Additionally, DMF integration enables microfluidic chip designers to realize topologies not possible with a purely passive chip. A DMF electrode array enable

“sandbox” chemical analyses to be performed. As such, experimenters may choose to configure the assay as an ELISA. In DMF ELISA applications, the use of high voltages to actuate droplets may fuel concerns about excess heat causing enzyme denaturation. Because of the very low internal resistance of each electrode pad, and the excellent insulation provided by the silicon substrate, there is no significant heat dissipation resulting from device use. The electrode array described here will pose no heat-related threat to the viability of enzymes. A temperature-controlled version of this assay may be implemented using a resistive electrode pad layer [12].

The DMF research presented here is by no means complete, and is subject to the following limitations, all of which are slated to be addressed in future research work. Firstly, it is still unclear what effect, if any, alternating current (AC) has on droplet actuation, and whether it is perceptibly superior to direct current (DC) when it comes to droplet actuation. While studies generally agree that an AC voltage source provides faster and more stable droplet actuation than a DC voltage source, the literature is careful to note that droplet actuation performance depends largely on the hydrophobic coating. The superiority of one source type over the other has yet to be tested on the assay described here.

## REFERENCES

1. Wang, S.; Ge, L.; Song, X.; Yu, J.; Ge, S.; Huang, J.; Zeng, F. *Biosens. Bioelectron.* 2012, *31*, 212–218.
2. Martinez, A. W. *Bioanalysis* 2011, *3*, 2589–2592.
3. Cheng, C. M., Martinez, A. W., Gong, J., Mace, C. R., Phillips, S. T., Carrilho, E., Mirica, K. A., Whitesides, G. M., *Angew. Chem., Int. Ed.* 2010, *49*, 4771–4774.
4. Hsu, C. –K., Huang, H. –Y., Chen, W. –R., Nishie, W., Ujiie, H., Natsuga, K., Fan, S. –T., Wang, H. –K., Lee, J. Y. –Y., Tsai, W. –L., Shimizu, H., Cheng, C. –M., *Anal. Chem.* 2014, *86*, 4605–4610.
5. Murdock, R. C., Shen, L., Griffin, D. K., Keely-Loughnane, n., Papautsky, I., Hage, J. A. *Anal. Chem.* 2013, *85*, 11634–11642.
6. Hsu, M. –Y., Yang, C. –Y., Hsu, W. –S., Lin, K. –H., Wang, C. –Y., Shen, Y. –C., Chen, Y. –C., Chau, S. –F., Tsai, H. –Y., Cheng, C. –M. *Biomaterials* 2014, 3729–3735.
7. Gonzalez, A., Gaines, M., Gallegos, L. Y., Guevara, R., Gomez, F. A., 2017, *Electrophoresis*, in press.
8. Samad, M. F.; Kouzani, A. Z.; Samad, M. *2013 ICME International Conference on Complex Medical Engineering* 2013.
9. Samad, M. F.; Kouzani, A. Z.; Hosain, M. K.; Magniez, K.; Islam, M. S.; Kaynak, A.; Das, S.; Alam, M. N. H. Z.; Moghadam, A. A. A. *2014 4th International Conference on Engineering Technology and Technopreneuship (ICE2T)* 2014.
10. Chevalliot, S.; Heikenfeld, J. *MRS Proceedings* 2011, 1346.
11. Klarman, D.; Andelman, D.; Urbakh, M. *Langmuir* 2011, *27* (10), 6031–6041.
12. Nelson, W. C.; Peng, I.; Lee, G.-A.; Loo, J. A.; Garrell, R. L.; Kim, C.-J. “*C. Analytical Chemistry* 2010, *82* (23), 9932–9937.